ORIGINAL PAPER

CrossMark

Strategies for Enhancing the Electrocatalytic Activity of M–N/C Catalysts for the Oxygen Reduction Reaction

Young Jin Sa[1] · Jinwoo Woo[1] · Sang Hoon Joo[1]

Abstract

The development of highly active and durable nonprecious metal catalysts that can replace expensive Pt-based catalysts for the oxygen reduction reaction (ORR) is of pivotal importance in polymer electrolyte membrane fuel cells. In this line of research, metal and nitrogen codoped carbon (M–N/C) catalysts have emerged as the most promising alternatives to Pt-based catalysts. This review provides an overview of recently developed synthetic strategies for the preparation of M–N/C catalysts to enhance the catalytic activity of the ORR. We present five major strategies, namely the use of metal–organic frameworks as hosts or precursors, the use of sacrificial templates, the addition of heteroelements, the preferential generation of active sites, and a biomimetic approach. For each strategy, the advantages capable of boosting catalytic activity in the ORR are summarized, and notable examples and their catalytic performances are presented. The ORR activities and measurement conditions of high-performing M–N/C catalysts are also tabulated. Finally, we summarize this review with some suggestions for future studies.

Keywords M–N/C · Electrocatalyst · Oxygen reduction reaction · Synthetic strategy

1 Introduction

The ever-increasing worldwide demand for clean energy carriers has resulted in increased attention to a "hydrogen economy" as a possible long-term solution for securing clean and renewable energy [1, 2]. Although a hydrogen economy offers a compelling picture of sustainable energy, significant scientific and technical challenges must first be circumvented to allow this vision to be fully implemented. In this context, one of the key factors dictating the overall efficiency of hydrogen-based energy cycles is the performance of the electrochemical energy conversion devices, for example, a fuel cell or a water electrolyzer [3–7].

As a low-temperature type of fuel cell, polymer electrolyte membrane fuel cells (PEMFCs) are zero-emission energy conversion devices that convert hydrogen fuel directly into electricity with high efficiency. The multiple advantages imparted by PEMFCs render them widely applicable for transportation, mobile, and stationary applications [8, 9]. In general, the performance of PEMFCs depends mainly on the efficiency of electrocatalysts for the oxygen reduction reaction (ORR) at the cathode. As the ORR proceeds via a proton-coupled, four-electron transfer, this reaction is sluggish; the intrinsic kinetics for the ORR are approximately million times slower than the hydrogen oxidation reaction taking place at the anode on a Pt catalyst [10]. To overcome the demanding kinetics of the ORR, high-loading Pt-based catalysts have been commonly employed for the PEMFC cathode [11]. However, Pt-based catalysts pose multiple drawbacks including high costs, the scarcity of Pt, declining activity with long-term operation, and susceptibility to poisoning. Indeed, Pt metal is solely responsible for 40–50% of the total cost of the PEMFC stack, which has limited the widespread application of PEMFC systems [12]. To address this issue, the development of nonprecious metal ORR catalysts has recently received increasing attention, and a diverse class of ORR catalysts, based on metal oxide/carbon composites [13–15], metal chalcogenides or metal carbides [16–18], transition metal and nitrogen codoped carbon (M–N/C) [19–23], and heteroatom-doped carbon [24, 25], has been pursued. Among these nonprecious metal catalysts,

✉ Sang Hoon Joo
  shjoo@unist.ac.kr

1 School of Energy and Chemical Engineering, Ulsan National Institute of Science and Technology (UNIST), 50 UNIST-gil, Ulsan 44919, Republic of Korea

the M–N/C catalysts are particularly noteworthy, primarily due to their high ORR activities.

The field of heterogeneous M–N/C catalysts has a history dating back more than 50 years. In 1964, Jasinski first demonstrated that cobalt phthalocyanine could catalyze the ORR in alkaline media, opening up the possibility of M–N/C catalysts as potential alternatives to Pt-based catalysts [26]. Since then, several types of metallomacrocyclic compounds, such as metalloporphyrins and metallotetraazaannulenes, have been widely explored as new M–N/C catalysts [27, 28]. However, the ORR activity and durability of these molecular catalysts were significantly lower than those of Pt-based catalysts. In the course of overcoming these issues, the preparative chemistry of M–N/C catalysts underwent several stages of breakthroughs. For example, Jahnke et al. suggested that the high-temperature heat treatment of metallomacrocyclic compounds could significantly improve the activity and durability of M–N/C catalysts [29]. The Yeager group demonstrated that a M–N/C catalyst prepared from a mixture of metal, nitrogen, and carbon precursors exhibited a comparable ORR activity to catalysts derived from expensive metallomacrocyclic compounds, thereby representing a more economical route towards M–N/C catalysts [30]. This method suggested a possibility of combining various precursors for each component, allowing for the more flexible design of M–N/C catalysts. However, despite continued research into the development of high-performance M–N/C catalysts prior to 2008, the ORR activities of M–N/C catalysts remained more than two orders of magnitude lower than those of Pt-based catalysts.

In 2009, a major breakthrough in the field of M–N/C catalysts was made by the Dodelet group [20]. They prepared Fe–N/C catalysts by filling microporous carbon black with ferrous acetate and 1,10-phenanthroline, followed by heat treatment under NH_3. The optimized Fe–N/C catalyst achieved a PEMFC volumetric current density of 99 A cm^{-3} at 0.8 V, which was ~ 35 times higher than that of the previously reported best-performing catalyst. Notably, this performance was close to the target of 130 A cm^{-3} set by the US Department of Energy (DOE) in 2010. Subsequently, in 2011, the Zelenay group developed a M–N/C catalyst based on Fe, Co, and polyaniline, which achieved a highly promising PEMFC durability up to 700 h at 0.4 V along with a high initial current density [21]. The results obtained by the Dodelet and Zelenay groups suggested the practical viability of M–N/C catalysts for PEMFC applications, and triggered a tremendous surge of research interest in this field. Consequently, significant progress has been made in the design and synthesis of M–N/C catalysts, as well as in the elucidation of the catalyst active sites [31–45]. The previous studies on the active sites of M–N/C catalysts provided a plausible evidence that the active sites contain atomically dispersed metal coordinated to N atoms (M–N_x sites). We note that the metal nanoparticles (NPs) encapsulated in carbon shells were suggested recently to exhibit a considerable ORR activity. However, the catalytic role of such NPs is still a matter of debate and is not discussed in this review.

The advances achieved in this field have been previously presented in a number of review papers. The developments in M–N/C catalysts prior to 2011 have been summarized in reviews by Zhang et al. [46], Dodelet and Zelenay et al. [47], Palacin et al. [48], and Zhang et al. [49]. In addition, recent reviews have focused on more specific aspects of M–N/C catalysts, such as molecular M–N/C catalysts [50], the active sites of M–N/C catalysts [51, 52], the role of transition metals in M–N/C catalysts [53], the catalytic mechanisms over M–N/C catalysts [54], and characterization of the M–N/C catalysts [55].

In this review, we focus on the synthetic strategies and preparative chemistry toward highly active and durable M–N/C catalysts developed since 2011. Although numerous methods are available that can boost the performance of M–N/C catalysts, we selected five major synthetic routes in this review: (i) the exploitation of metal–organic frameworks (MOFs) as hosts or precursors, (ii) the use of sacrificial templates, (iii) the addition of heteroelements, (iv) the preferential generation of active sites, and (v) biomimetic approaches. We explain the advantages of each strategy and present notable examples with their ORR activities and/or PEMFC performances. We also summarize the catalytic activities and measurement conditions of high-performing M–N/C catalysts for the ORR. For a summary regarding the PEMFC performances of M–N/C catalysts, readers are encouraged to refer the recent review by Shao and Dodelet [56]. Finally, we conclude this review with a summary and some suggestions for future studies.

2 Thermal Conversion of Metal–Organic Frameworks

MOFs are crystalline porous materials composed of inorganic species (metal ions or clusters) that are bridged by organic ligands [57, 58]. MOFs generally exhibit large surface areas up to few thousand m^2 g^{-1}, and they can be constructed from a myriad of compositions. Although the use of MOFs themselves as electrocatalysts is limited due to their intrinsically low electrical conductivities, the high-temperature pyrolysis of MOFs can convert the organic ligands into porous carbon to endow conductivity to the resulting materials, thereby enabling their utilization as M–N/C catalysts [59]. In the conversion of MOFs to M–N/C catalysts, MOFs can be utilized as microporous hosts for metal and nitrogen precursors, or as metal and nitrogen precursors.

2.1 MOFs as Hosts

When MOFs are employed as hosts, the metal and nitrogen precursors are initially impregnated into the micropores of the MOFs, and are later transformed into active sites through their reaction within the micropores during subsequent pyrolysis. The most widely used MOF for this purpose is zeolitic imidazolate framework-8 (ZIF-8), in which Zn^{II} centers are connected to the N atoms of imidazolate ligands. During pyrolysis of ZIF-8, Zn is eliminated in situ due to the low boiling point of metallic Zn (i.e., 907 °C), thus yielding a highly porous carbon structure after pyrolysis. Furthermore, the imidazolate ligands can serve as an additional source of nitrogen.

The utilization of ZIF-8 as a microporous host was first demonstrated by Dodelet et al. in the preparation of high-performance Fe–N/C catalysts [60]. In their work, ZIF-8 was initially impregnated with ferrous acetate (Fe precursor) and 1,10-phenanthroline (N and C precursor), dried, ball-milled, and finally pyrolyzed under Ar and then under ammonia gas. The resulting catalyst was composed of nitrogen-containing microporous carbon hosting Fe–N_x active sites (Fig. 1a). The membrane electrode assembly (MEA) employing the optimized Fe–N/C catalyst at the cathode exhibited a current density of 1.2–1.3 A cm^{-2} at 0.6 V with a peak power density of 0.91 W cm^{-2} in PEMFC. The MEA exhibited the highest volumetric activity (230 A cm^{-3} at 0.8 V) at that time,
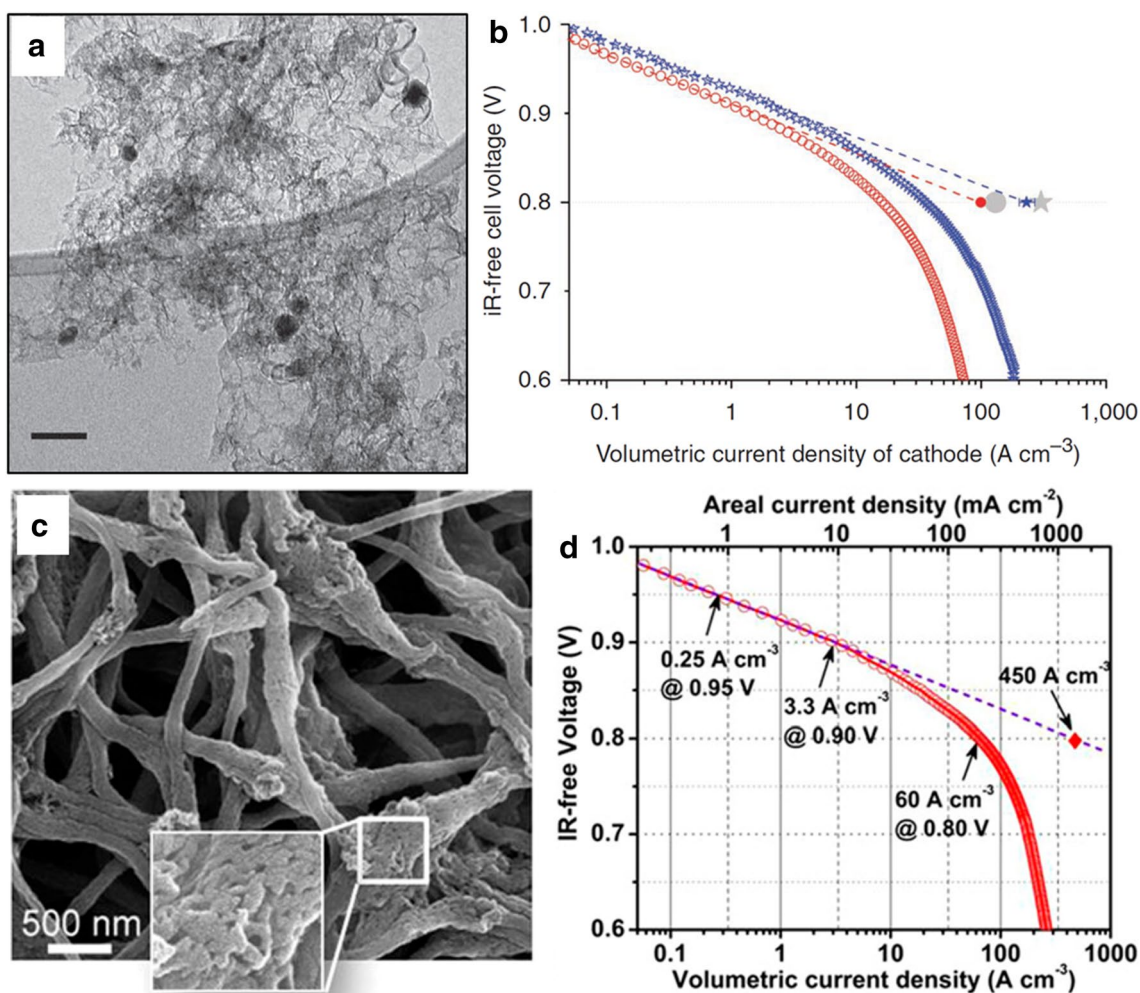
Fig. 1 **a** TEM image of the optimized Fe–N/C catalyst by using ZIF-8 as the host (scale bar: 50 nm). **b** Comparison of the iR-free polarization curve of the optimized Fe–N/C catalyst (hollow blue stars) with that of the previously reported best-performing catalyst (hollow red circles) in a H$_2$–O$_2$ PEMFC operated at 80 °C. The solid blue stars and red circles indicate the extrapolated volumetric current densities at 0.8 V for each catalyst. The gray star and circle represent the 2020 target (2015 target at that time) and 2010 target set by the US DOE, respectively. **c** Scanning electron microscopy image of the nanofibrous Fe–N/C catalyst. **d** iR-free polarization curve of the catalyst in a H$_2$–O$_2$ PEMFC operated at 80 °C. The red diamonds represent the extrapolated volumetric current density at 0.8 V. Reproduced with permission from [60]. Copyright (2011) Nature Publishing Group (a, b); Reproduced with permission from [64]. Copyright (2015) National Academy of Sciences (c, d)

which exceeded the US Department of Energy (DOE) 2010 activity target of 130 A cm^{-3} (Fig. 1b). This volumetric current density was ~ 2.3 times higher than the MEA made by their previously reported catalyst [20], which was prepared according to a similar procedure, but without the use of a microporous ZIF-8 host, thereby highlighting the beneficial role of MOFs in preparing advanced M–N/C catalysts.

In the synthesis of Fe–N/C catalysts using ZIFs as the microporous support, the structural properties of ZIFs have significant influences on the PEMFC performance [61–63]. To examine this effect, Jaouen et al. prepared Fe–N/C catalysts using nine Zn-based ZIFs with different topologies, Zn/N/C contents, and textural properties [63]. They found that the PEMFC performances of the catalysts correlated linearly with the cavity size and the specific surface area of the parental ZIF supports. In addition, higher activities originated from larger numbers of Fe–N$_x$ active sites, as evidenced by Mössbauer spectroscopy. It was suggested that the reaction of Fe and N precursors is promoted inside larger cavities, leading to the formation of more abundant Fe–N$_x$ sites [63].

Liu et al. developed a nanofibrous Fe–N/C catalyst from pyrolysis of electrospun polymer mixture containing polyacrylonitrile (PAN), an Fe(II)-based organometallic precursor, and the ZIF (Fig. 1c) [64]. This catalyst design utilizes both the high active site density achieved by the ZIF host and the excellent electronic conductivity of the PAN-derived graphitic carbon fiber. In addition, the macroporous voids generated between the carbon fiber networks could facilitate mass transport. This catalyst exhibited very high PEMFC performance with the highest reported volumetric activity of 450 A cm^{-3} at 0.8 V, which far exceeded the 2020 DOE target, i.e., 300 A cm^{-3} (Fig. 1d). These results suggest that the microporous–macroporous hierarchical structural design is critical to enhancing in the MEA performances of Fe–N/C catalysts [64].

In addition to the Zn-based ZIF family, the Zn/aminoterephthalate-based MOF (IRMOF-3) [65], a magnesium/naphthalenedicarboxylate-based anionic MOF [66], and a copper/benzenetricarboxylate-based MOF (HKUST-1) [67] were also employed as porous hosts for metal and nitrogen precursors. However, the organic ligands of these MOFs contain oxygen instead of nitrogen, and therefore may be inappropriate for preparing highly active M–N/C catalysts. For this reason, N-rich imidazolate-based ZIFs are most commonly employed for the preparation of M–N/C catalysts. For oxygen-ligand-based MOFs, ligands are often aminated to impart N-containing functionality, with the MIL-NH$_2$ series being one such example [68–70].

## 2.2 MOFs as All-in-One Precursors

MOFs composed of ORR-active metals (i.e., Fe and Co) and N-containing ligands can serve as all-in-one precursors for the three components of M–N/C catalysts. In this case, a simple pyrolysis of MOFs without the impregnation and drying steps simplifies the preparation process. Importantly, inherent M–N bonding in the parental MOF can be directly translated into active M–N$_x$ species in the final M–N/C catalysts. Due to these advantages, this strategy has emerged as a simple yet efficient methodology for preparing high-performance M–N/C catalysts. In addition, owing to the wide tunability of the metal and the ligands, a variety of MOF precursors have been investigated, including Fe-imidazolate frameworks [71–79], Co-imidazolate frameworks [80–96], Prussian blue [97–101], and other families of MOFs [102–105].

The use of MOFs as all-in-one precursors was first realized by Liu et al., who synsesized Co–N/C catalysts by the simple pyrolysis of a Co-imidazolate framework (Co-ZIF) [80, 81]. This Co-ZIF (ZIF-67) is composed of Co^{II} sites tetrahedrally coordinated to four N atoms of the imidazolate ligands (Fig. 2a). They suggested that the thermal activation of ZIF-67 at 750 °C transformed the original Co–N$_4$ structure into ORR-active Co–N$_x$ sites (Fig. 2b). Thermal activation and successive acid-leaching resulted in a Co–N/C catalyst with a half-wave potential of 0.68 V (vs. reversible hydrogen electrode, RHE) in 0.5 M H$_2$SO$_4$ [81]. In a similar strategy, the Liu group prepared a porphyrin-based porous organic polymer (POP) with a three-dimensional (3D) network structure and a high surface area of ~ 2300 m^2 g^{-1} [106]. Heat-treatment of the Fe porphyrin-based POP produced a highly active catalyst both in the half-cell configuration and in the PEMFC. This POP-conversion method has therefore provided active M–N/C catalysts in an analogous way to MOF-based synthetic methods [106–109].

Recently, the Mai group produced a polyhedral Co–N/C catalyst exhibiting multimodal pores between CNT bundles [96]. During the preparation of this catalyst, the two-step pyrolysis of ZIF-67 was carried out. The first heat-treatment at a relatively low temperature created metallic Co NPs, which catalyzed the formation of the CNT bundles during the second high-temperature pyrolysis step. The final optimized Co–N/C catalyst exhibited a high ORR activity comparable with that of Pt/C in an alkaline electrolyte [96].

In the majority of MOF-derived synthetic routes to M–N/C catalysts, not only catalytically active M–N$_x$ species, but high amounts of undesirable large metal-based NPs were also generated. This phenomenon can be attributed to the excess quantities of metals present in MOFs (e.g., ~ 20 wt% Co in ZIF-67), compared to the metallic contents required for preparation of the high-performing M–N/C catalysts (i.e., ~ 0.5–3 wt%). This high density
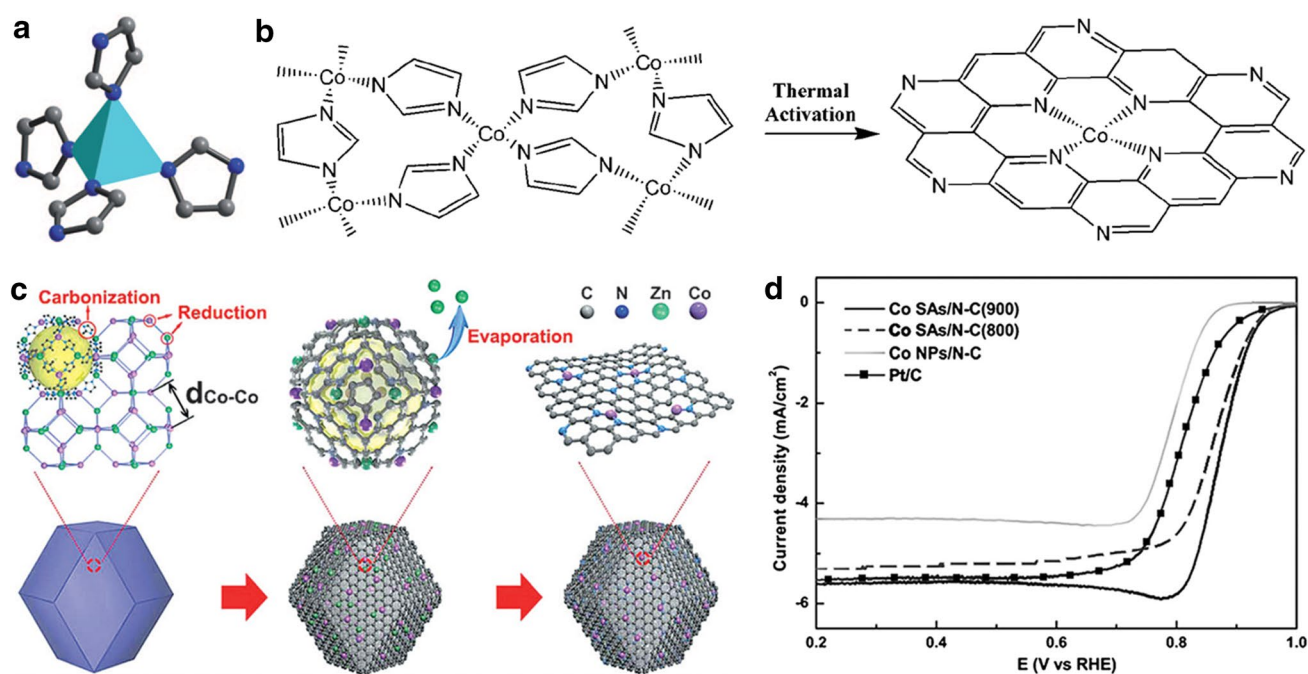
Fig. 2 **a** The tetrahedral Co–N$_4$ unit structure of ZIF-67. **b** Schematic illustration of the suggested structural evolution of Co–N$_x$ active sites during thermal activation of a Co-based ZIF. **c** Schematic illustration of the preparation of the Co–N/C catalyst (Co SAs/N–C) in the presence of Co–N$_x$ sites derived from ZIF-67. **d** ORR polarization curves of Co SAs/N–C, Co NPs/N–C, and Pt/C in 0.1 M KOH. Reproduced with permission from [81]. Copyright (2011) Wiley-VCH Verlag GmbH & Co. KGaA (a, b); Reproduced with permission from [90]. Copyright (2016) Wiley-VCH Verlag GmbH & Co. KGaA (c, d)

of metal atoms consequently increases the probability of aggregation at elevated temperatures. To address this issue, the Li group introduced Zn^{2+} ions as "fence" atoms in Co-based ZIFs to expand the adjacent distances of Co atoms, thereby reducing the possibility of Co aggregation [90]. During pyrolysis, the Zn atoms were evaporated, to leave predominantly Co–N$_x$ sites in the pyrolyzed material (Fig. 2c). The resulting active site-rich catalyst exhibited a superior ORR activity to both the Co NP-abundant catalyst and a commercial Pt/C catalyst (Fig. 2d) [90].

Furthermore, Chen et al. prepared Fe–N/C catalysts derived from the thermal conversion of Fe-doped ZIF-8 with various Fe/(Fe + Zn) ratios ranging from 5 to 25 wt% [78]. They found that higher quantities of Fe atoms in the precursor led to the formation of larger quantities of Fe and Fe$_3$C NPs, while the 5 wt%-loaded ZIF-8 produced a catalyst containing only Fe–N$_x$ sites. This method greatly improved the ORR activity, with a 130 mV increase in the half-wave potential [78]. The Li group also recently demonstrated that precursor pyrolysis in the presence of a small quantity of Fe (i.e., 0.8 wt% in the precursor) produced exclusively Fe–N$_x$ active sites [79]. Upon increasing the Fe loading to 4 wt%, large quantities of Fe and Fe$_3$C NPs were formed, and the ORR activity diminished considerably with a 60 mV negative shift in the half-wave potential [79].

## 3 Use of Sacrificial Templates

Enlarging the surface area of a catalyst is a direct method to increase the number of active sites on the catalyst surface, and enhance the ORR activity. M–N/C catalysts are typically synthesized via the high-temperature pyrolysis of precursor mixtures, which is critical to creating active M–N$_x$ sites as well as to endowing a high electrical conductivity. However, this pyrolysis step commonly results in structurally ill-defined, low surface area catalysts. The use of sacrificial templates can therefore provide a straightforward method for the production of M–N/C catalysts with large surface areas and controlled porosity [110–139]. In addition, well-defined nanostructures can be generated according to the type of template employed. In the template-based method, a precursor in the gas, liquid, or solid phase is initially introduced into the pores or adsorbed onto the surface of a template, and this is followed by carbonization at high temperatures. Finally, the template is removed by an etchant to generate the porous structure. For this purpose, a variety of templates have been examined including silica [110–125], metal oxides [126–130], nanowires [131–135], and sodium chloride (NaCl) [136–139].

3.1 Silica Templates

Silica is stable at high temperatures and is easily etched by NaOH or HF. In addition, preparation methods towards various types of silicas, including colloidal silica NPs and mesoporous silica, have been well established. As such, the silica-templating method has been widely investigated for the fabrication of porous M–N/C catalysts. For example, the Atanassov group utilized fumed silica (porous branched silica) as the sacrificial support with a variety of precursors, including macrocyclic compounds [110] and organic molecules [111–113] to produce M–N/C catalysts with spherical mesopores of few ten nanometers in diameter. The use of larger templates, such as silica microparticle templates, yielded porous open structured capsule-type M–N/C catalysts with few hundred nanometer pores [114, 115].

Ordered mesoporous silica (OMS) has attracted particular attention because of its periodic, uniform, and tunable pore structure. For example, Joo et al. developed a solid-state hard-templating synthetic method using metal-loporphyrins as the all-in-one precursor and OMSs as the templates (Fig. 3a) [117]. In this process, the solid-state mixing of a metalloporphyrin and SBA-15, followed by pyrolysis and silica etching produced in metal-doped ordered mesoporous porphyrinic carbon (M-OMPC, M = Fe, Co,

FeCo, etc.). This solid-state infiltration method is simple and rapid compared to the typical wet-impregnation method, as the latter employs an additional drying step that often requires further optimization. Interestingly, the obtained M-OMPC catalysts had hierarchical micropores (~ 1 nm) and mesopores (4–20 nm), and exhibited large surface areas of 1000–1500 $m^2 g^{-1}$, which can expose a high density of catalytically active M–N_x sites. Among the family of M-OMPC catalysts, FeCo-OMPC exhibited a particularly high ORR activity in acidic media (0.1 M $HClO_4$) with a half-wave potential at 0.85 V (vs. RHE), which compared favorably to commercial Pt/C catalysts (Fig. 3b). In addition, this solid-state templating method also successfully produced replicated M–N/C structures from KIT-6 (a further type of OMS) and mesocellular-foam silica [117].

Similarly, other precursors, such as metal phthalocyanines [120, 123, 124], metal-polyaniline complexes [116, 122], and metal-phenanthroline complexes [121] were successfully employed as precursors for mesoporous M–N/C catalysts. Müllen et al. used vitamin B12 as the Co, N, and C precursor and montmorillonite (a layered clay), SBA-15, and silica colloids as sacrificial templates [118]. The three obtained catalysts exhibited well-developed pore structures, with the silica colloid-based catalyst exhibiting the largest surface area, followed by the SBA-15- and
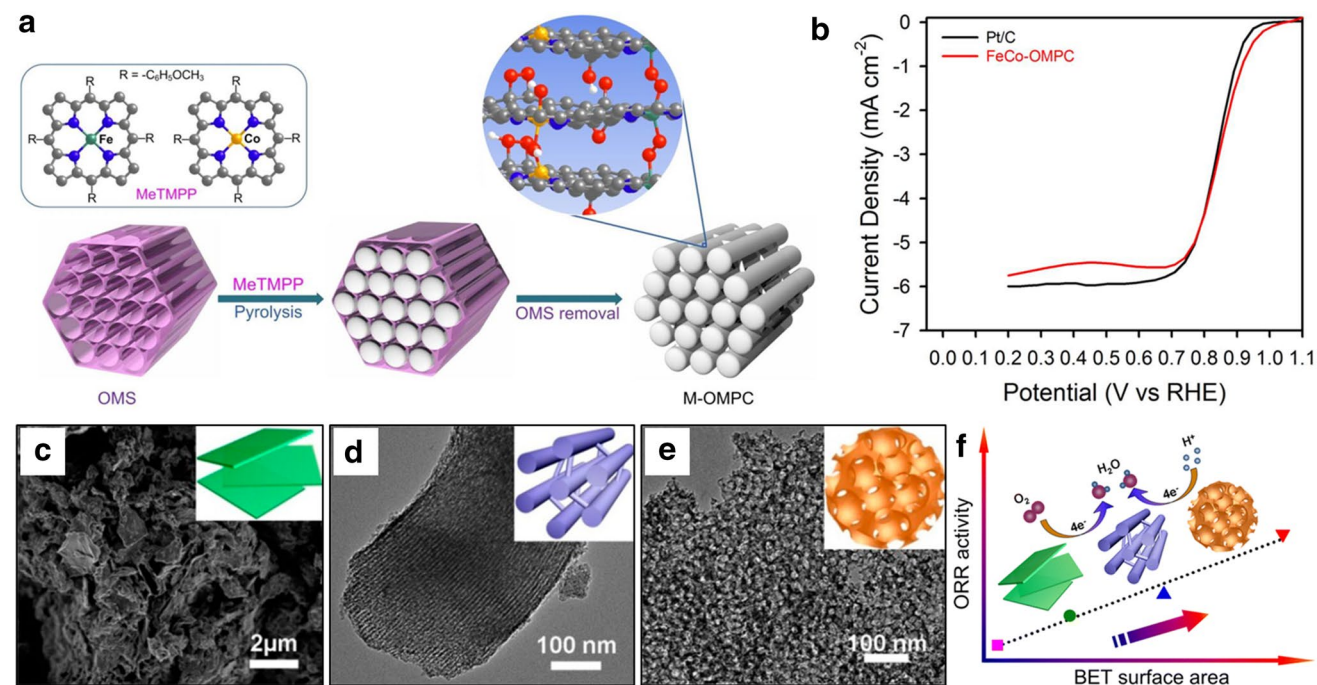
Fig. 3 **a** Schematic illustration of the synthesis of M-OMPC catalysts by the solid-state hard-templating method using OMS, and a suggested model of FeCo-OMPC. The yellow, cyan, red, blue, grey, and white spheres represent Co, Fe, O, N, C, and H atoms, respectively. **b** Polarization curves of FeCo-OMPC and a commercial Pt/C catalyst measured in 0.1 M $HClO_4$. TEM images of Co–N/C catalysts templated from **c** montmorillonite, **d** SBA-15, and **e** silica colloids using vitamin B12 as a precursor. **f** Linear correlation between the BET surface areas of the templated Co–N/C catalysts and their ORR activities. Reproduced with permission from [117]. Copyright (2013) Nature Publishing Group (a, b); Reproduced with permission from [118]. Copyright (2013) American Chemical Society (c–f)

montmorillonite-templated catalysts (Fig. 3c–e). The ORR activities of the catalysts correlated linearly with their Brunauer–Emmett–Teller (BET) surface areas, thereby highlighting the importance of surface area in the electrocatalytic process (Fig. 3f) [118].

3.2 Metal Oxides as the Reactive Templates

Metal oxide nanostructures based on ORR-active metals such as Fe and Co can serve both as sacrificial templates and as a source of the metal species during the preparation of M–N/C catalysts [126–130]. For example, Chen et al. took advantage of $Fe(OH)_3$ as a volatile template containing an Fe source [126]. They combined 2-fluoroaniline and $FeCl_3$ to form a poly(fluoroaniline)-$Fe(OH)_3$ hybrid, and the subsequent pyrolysis of this composite produced a porous Fe–N/C catalyst free from Fe-based particles. They suggested that $Fe(OH)_3$ is dehydrated to form FeO(OH) which subsequently undergoes reductive transformation to Fe_2O_3 → Fe_3O_4 → Fe in situ by adjacent carbon atoms at high temperatures. The reduced Fe then reacts with the HCl produced from the Cl^- ions bonded to poly(fluoroaniline) to generate $FeCl_3$ that was subsequently sublimated. The resulting catalyst exhibited a half-wave potential of 0.80 V (vs. RHE) in 0.1 M KOH [126]. In addition, Zhang et al. employed a similar approach using porous Fe_3O_4 microspheres as the template [127]. In this case, the Fe_3O_4 microspheres were coated with polypyrrole with the aid of cetyltrimethylammonium bromide. Subsequent pyrolysis of the composite at 950 °C produced the desired impurity-free porous Fe–N/C microspheres, which exhibited a high BET surface area ($674 \text{ m}^2 \text{ g}^{-1}$) and a half-wave potential of 0.86 V (vs. RHE) in 0.1 M KOH [127].

Recently, Dong et al. prepared a porous cubic graphitic carbon framework using Fe_3O_4 nanocube superlattice [130]. In this system, pre-synthesized Fe_3O_4 nanocubes capped with an oleic acid surfactant were self-assembled to form a superlattice structure. During the thermal annealing step, oleic acid was converted into a graphitic carbon framework and the Fe atoms from the Fe_3O_4 nanocubes diffused into the carbon layer. Subsequent acid-leaching and heat-treatment under NH_3 produced the desired Fe- and N-doped carbon framework structure (Fig. 4a). Thus, in this protocol, the Fe_3O_4 nanocubes served both as the sacrificial template and the Fe source. The resulting Fe–N/C catalyst exhibited a highly ordered porous network with a large BET surface area of $1180 \text{ m}^2 \text{ g}^{-1}$ (Fig. 4b). In addition, the active sites of the catalyst were predominantly Fe–N_x (~3 wt% Fe), as evidenced by X-ray diffraction (XRD), transmission electron microscopy (TEM), and X-ray absorption spectroscopy (XAS). The high surface area and active site density of this material contributed to an excellent ORR activity with a

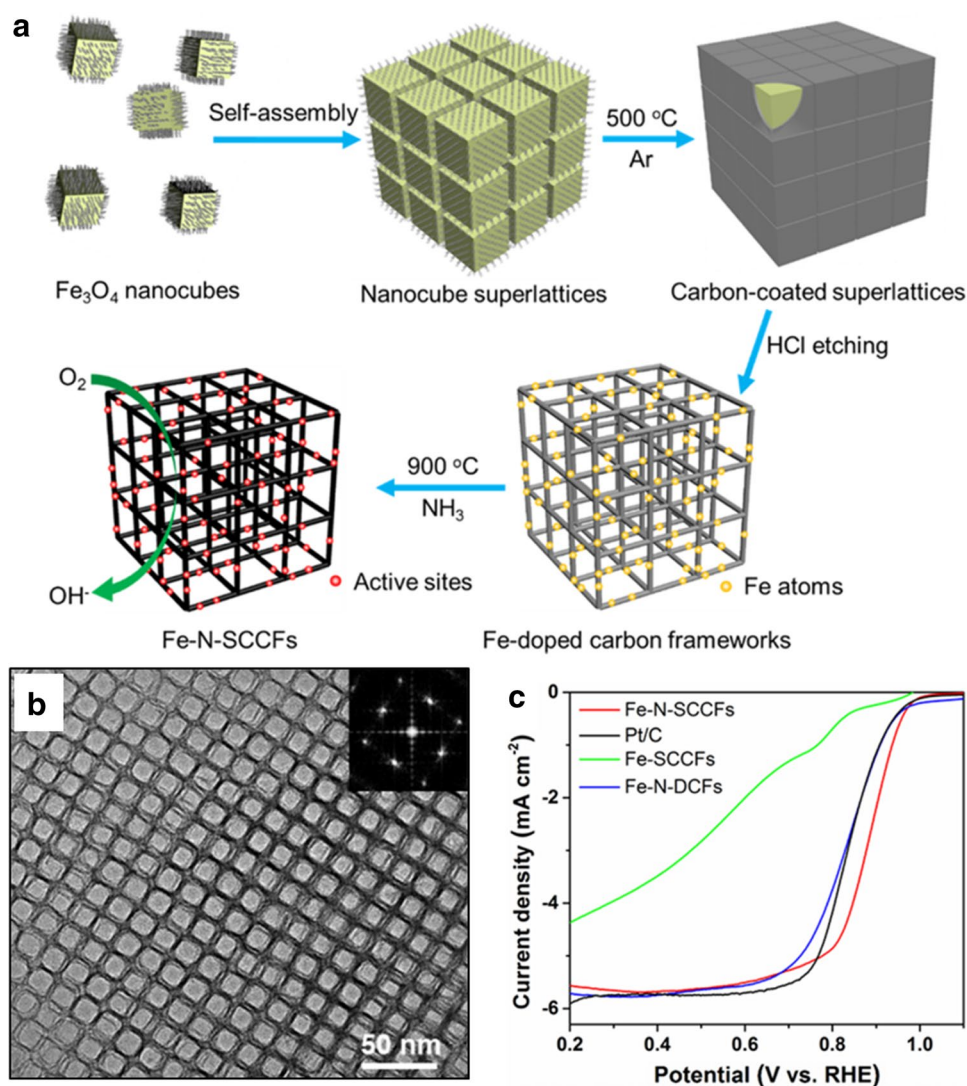half-wave potential of 0.883 V in 0.1 M KOH (Fig. 4c) [130].

3.3 Other Sacrificial Templates

The exploration of new types of sacrificial templates has allowed the production of unique nanostructured M–N/C catalysts. For example, tellurium nanowires (Te NWs) have been demonstrated as useful supports for the construction of tubular fiber M–N/C catalysts. Due to the relatively low boiling temperature of Te (~ 450 °C [140]), Te NW templates are removed in situ during the pyrolysis stage without any additional process. The Yu group demonstrated the Te NW-templated synthesis of porous fiber Fe–N/C catalysts [131]. A mixture of glucosamine/ferrous gluconate was hydrothermally treated with Te NWs to polymerize the components onto the surface of the NWs. They emphasized the importance of employing an Fe^{II} precursor rather than an Fe^{III} precursor, as the latter rapidly oxidizes Te, leading to the collapse of the fibrous structure of the product [131]. Similarly, Lin et al. developed a Fe-glucosamine-derived nanotube (NT) catalyst with well-dispersed Fe–N_x sites [132]. The Manthiram group utilized Te NTs as the sacrificial template and ZIF-8 as the microporous host for the precursors [135]. In this case, ZIF-8 was grown on the porous Te NTs, prior to coating with Fe-polydopamine. Pyrolysis at 950 °C vaporized the majority of Zn present in the ZIF-8 and the Te NTs, leading to a highly porous and tubular Fe–N/C catalyst with a BET surface area of $1380 \text{ m}^2 \text{ g}^{-1}$ (Fig. 5a, b) [135]. This strategy was also demonstrated for Co-doped ZIF precursor to yield Co–N/C catalysts [134].

NaCl can also function as a structure directing agent, and is particularly useful in the preparation of M–N/C catalysts with two-dimensional (2D) sheet morphologies. This NaCl-based templating method has a number of advantages: (i) the synthesis is scalable and economic, as NaCl is inexpensive and can be easily collected and recycled; (ii) this method allows the formation of Fe-based particles to be suppressed due to the in situ generation and volatilization of $FeCl_x$ species in the presence of NaCl; and (iii) template removal is simple and can be carried out in neutral conditions, thereby avoiding degradation of the active sites In this context, Hu et al. synthesized carbon nanosheet-nanotube composite catalysts [138], in which the pyrolysis of an $Fe(NO_3)_3$-glucose-melamine mixture in the presence of a NaCl template led to the formation of CNT–carbon nanosheet hybrids (Fig. 5c). The resulting carbon nanosheet-nanotube catalyst contained a larger number of Fe–N_x sites and a better-developed pore structure than the untemplated catalyst, thereby resulting in a high ORR activity with a half-wave potential of 0.87 V (vs. RHE) in 0.1 M KOH [138]. Furthermore, Sung et al. employed Fe^{II} phthalocyanine as a precursor and NaCl as a template to produce a nanosheet Fe–N/C catalyst with
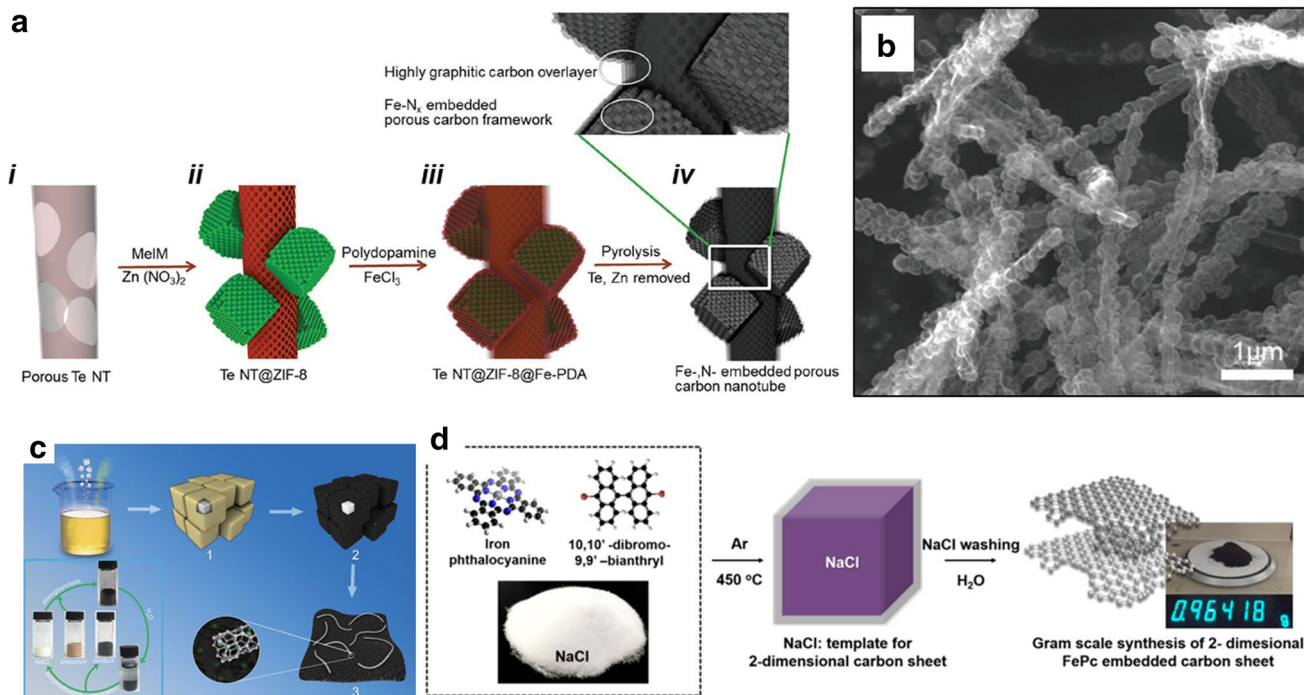
4 Addition of Heteroelements

Although the origin of synergistic effect is still unclear, heteroatom-doping has been effective to enhance the ORR activity of M–N/C catalysts. It is often the case that a bimetallic M_1M_2–N/C outperforms each monometallic catalyst [109, 111, 117, 141–145]. The other promotion effect could be found when sulfur (S) is doped into M–N/C catalysts [146–155]. This section introduces representative recent works that demonstrated the activity improvement by the addition of secondary metal or S.

4.1 Addition of Secondary Transition Metal

In the context of bimetallic synergy, Atanassov et al. investigated the impact of secondary metal for FeCo–, FeCu–, FeNi–, and FeMn–N/C catalysts [111]. They found that all catalysts possessed similar surface areas and pore structures, and that synergistic increase in the ORR activity was only

well-dispersed and structurally defined Fe–N_4 sites, enabled by low temperature treatment [139]. This was achieved through polymerization in the presence of 10,10′-dibromo-9,9′-bianthryl at 450 °C, and subsequent removal of NaCl by washing with H_2O (Fig. 5d) [139]. However, mechanism of the formation of the sheet-like morphology with NaCl-templated catalysts remains unclear, and further studies are required to investigate these points in greater detail.

Alternatively, Wei et al. used NaCl as a "shape fixing" template [136]. They created Fe-polyaniline complex nanostructures and fully sealed the precursor in NaCl via repeated recrystallization. During the pyrolysis stage, NaCl acted as a nanoreactor to prevent the collapse of the initial polymer nanostructures. In addition, gaseous products evolving during pyrolysis step generated the desired porosity, and N-containing gases reacted with Fe to increase the active site density. The use of this trapped synthetic system also reduced weight loss during the heat-treatment, thereby indicating that NaCl also could facilitate carbonization [136].

Fig. 5 **a** Schematic representation of the synthesis of porous and tubular Fe–N/C catalysts using Te NWs as templates and ZIF-8 as the microporous host, and **b** TEM image of the obtained catalyst. **c** Schematic illustration of the NaCl-templated synthesis of Fe–N/C catalyst constructed with CNT–carbon nanosheet hybrids. **d** Schematic illustration of the preparation of the 2-dimensional Fe–N/C catalyst shown for the FeMn–N/C catalyst (Fig. 6a). The other bimetallic catalysts exhibited similar or less active ORR activity than its monometallic counterpart, whereas the 4-electron selectivity was always enhanced in bimetallic systems [111]. In the case of M-OMPC catalysts (introduced in "Sect. 3.1"), using Fe phthalocyanine as the precursor and NaCl as the template. Reproduced with permission from [135]. Copyright (2017) Wiley-VCH Verlag GmbH & Co. KGaA (a, b); Reproduced with permission from [138]. Copyright (2016) The Royal Society of Chemistry (c); Reproduced with permission from [139]. Copyright (2011) American Chemical Society (d)

FeCo-OMPC exhibited an improved ORR activity compared to both Fe- and Co-OMPC in acidic media [117]. Müllen et al. also observed a Fe–Co promotion effect when the catalysts were prepared by the pyrolysis of polymeric porphyrin [141]. In their catalysts, although the active site densities in
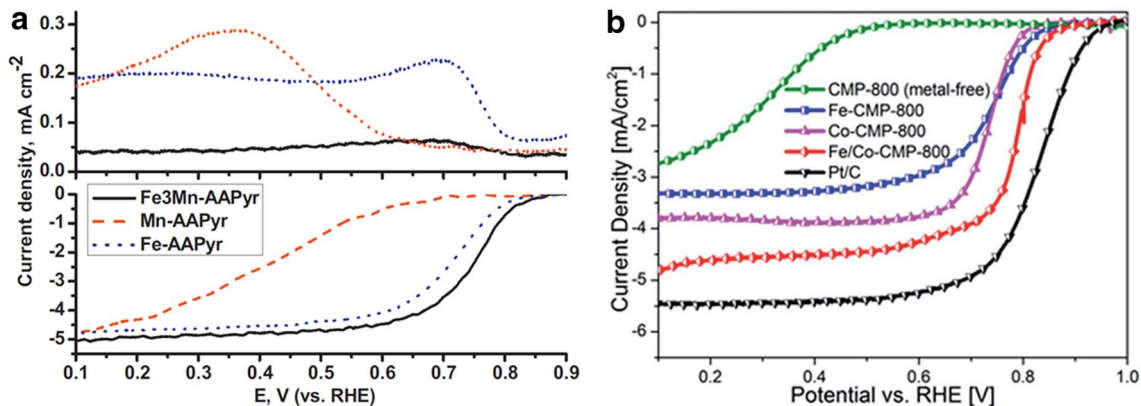
Fig. 6 **a** ORR polarization curves of monometallic and bimetallic (Fe, Mn)–N/C catalysts derived from 2-aminoantipyrine, measured in 0.5 M H_2SO_4. **b** ORR polarization curves of monometallic and bimetallic (Fe, Co)–N/C catalysts obtained by pyrolyzing porphyrin polymers measured in 0.5 M H_2SO_4. Reproduced with permission from [111]. Copyright (2012) Elsevier (a); Reproduced with permission from [141]. Copyright (2015) The Royal Society of Chemistry (b)

Fe–N/C and FeCo–N/C were comparable, the FeCo–N/C catalyst exhibited a 40 mV positive half-wave potential for the ORR in acidic media (Fig. 6b) [141]. In contrast to the observations made by the Atanassov group, this bimetallic catalyst was less selective to the 4-electron ORR than the Fe–N/C catalyst. We note that the co-existence of Fe and Co in M–N/C catalyst does not always enhance the ORR activity [156].

To date, the bimetallic synergy effect has not yet been clearly understood. This can be attributed to the heterogeneity of the active sites in M–N/C catalysts, which are formed mainly through high-temperature pyrolysis. Nevertheless, a number of explanations have been tentatively suggested, including a change in the catalyst structures during pyrolysis caused by the presence of a secondary metal, and the tuned electronic and local geometric structures of the active sites. In this regard, Strasser et al. prepared a polyaniline-based FeMn–N/C catalyst [143], which exhibited an enhanced ORR activity compared to its respective monometallic catalysts in an alkaline electrolyte, but a poorer activity compared to the Fe–N/C catalyst in an acidic electrolyte. They also conducted CO chemisorption experiments at low temperatures as well as temperature-programmed desorption (TPD) experiments, to quantify the active site density and to investigate the interactions between the M–N_x sites and CO molecules. The observed peak shift in the TPD profile suggested a stronger binding between CO molecules and the Fe–N_x sites in FeMn–N/C than those in the Fe–N/C. Given Mössbauer spectroscopy evidenced no alloy-like interactions between Fe and Mn, the TPD result suggested structural modification of the Fe–N_x active sites by addition of Mn. This modification led to 20 and 150% higher turnover frequencies (TOFs) of the bimetallic catalyst compared to the Fe–N/C catalyst in alkaline and acidic media, respectively [143].

4.2 Addition of Sulfur

The addition of sulfur has also been proven effective in enhancing the ORR activity of M–N/C catalysts, with the majority of S-promoting effects being demonstrated for Fe–N/C catalysts. The most prominent studies were performed by Herrmann and Kramm et al., who systematically investigated the role of elemental S as an additive during the pyrolysis of CoTMPP and FeTMPPCl with Fe oxalate (a pore-forming agent) [146–148]. They revealed that the addition of S exerts a number of positive effects: (i) the favorable formation of acid-leachable FeS_x species instead of insoluble FeC_x@C species; (ii) the generation of an amorphous carbon matrix (i.e., higher catalyst surface area) with extended graphene layers; and (iii) a change in the electronic structure of the active Fe–N_x sites.

The sulfur promotion effect was also demonstrated with the Zelenay group's polyaniline-based Fe–N/C catalyst, for which ammonium peroxydisulfate, $(NH_4)_2S_2O_8$, was added to oxidatively polymerize the aniline monomers [149]. The ORR activity was improved upon the addition of an optimal amount of $(NH_4)_2S_2O_8$. For S-containing catalysts, lower quantities of FeC_x and higher quantities of porphyrin type Fe–N_4 active sites were detected by XAS than S-free catalysts [149]. In addition, Cho et al. explained the enhanced ORR activity of S-doped Fe–N/C catalysts by the lowered work function, which facilitates electron transfer from the catalyst to O_2 [155, 157].

The selection of suitable precursors containing both S and N atoms could result in high-performance S-doped Fe–N/C catalysts. This enables more intimate contact between the Fe, N, and S atoms, and therefore maximizes the S-promotion effect compared to when the S source is separately mixed. For example, He and Liu et al. designed a thiolated polyacrylonitrile telomer; that is fluidic at room temperature, thereby enabling good contact with the Fe ions [150]. S-containing catalyst exhibited an improved ORR activity than S-free catalyst. They revealed the presence of FeN_xC_x species without any Fe–S species using time-of-flight secondary ion mass spectrometry, indicating the S-promotion effect did not originated from Fe–S bond [150]. In addition, the Strasser group used a S- and N-containing ionic liquid as a precursor for S-doped Fe–N/C catalysts [151]. They systematically investigated the role of other heteroatoms (i.e., phosphorus and boron) in the ORR activity of doped Fe–N/C catalysts, but found that only S had a positive influence on the activity (Fig. 7a), resulting a high ORR activity with a half-wave potential of 0.88 V (vs. RHE) in 0.1 M KOH, which is greater than a commercial Pt/C catalyst [151].

Finally, Sun et al. investigated the promotion effect of S-doping when the chloride ions in the $FeCl_3$ precursor were replaced by the thiocyanate (SCN^-) anion [152]. In this case, an excellent ORR activity was achieved in acidic media with a half-wave potential at 0.84 V (vs. RHE) (Fig. 7b) in addition to the highest reported PEMFC performance in terms of the maximum power density (1.03 W cm^{-2}) [152].

5 Preferential Formation of M–N_x Active Sites

Since the beneficial effects of high-temperature heat treatments on the ORR activities and the stabilities of M–N/C catalysts were demonstrated [29, 30], the pyrolysis step has been considered crucial and the majority of M–N/C catalysts are now prepared by the pyrolysis of macrocycles or precursor mixtures. During the pyrolysis step, catalytically active M–N_x sites dispersed on a carbon support are generated, thereby endowing catalytic activity towards the ORR.
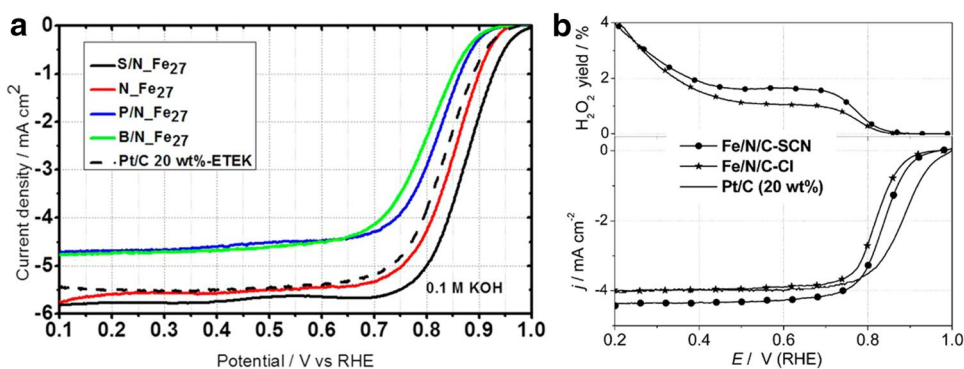
Fig. 7 a ORR polarization curves of the ionic liquid-derived heteroatom-doped Fe–N/C catalysts measured in 0.1 M KOH. **b** ORR polarization curves of the Fe–N/C catalysts prepared using Fe^{III} thiocyanate (denoted as Fe/N/C–SCN) and Fe^{III} chloride (denoted as Fe/N/C–Cl) measured in 0.1 M H_2SO_4. Reproduced with permission from [151]. Copyright (2014) American Chemical Society (a); Reproduced with permission from [152]. Copyright (2015) Wiley-VCH Verlag GmbH & Co. KGaA, Weinheim (b)

However, high-temperature heat treatment also induces the aggregation of metal atoms into less active large metal and/or metal carbide NPs, leading to the loss of M–N_x active sites in the resulting catalysts and an accompanying loss in ORR activity. As such phenomena are generally uncontrollable, the majority of heat-treated products possess a significant portion of inactive NPs. Furthermore, these NPs catalyze the Fischer–Tropsch reaction in situ at high temperatures, and so become coated with graphitic carbon shell that prevents the NPs from being acid-leached [17, 18].

In order to remove NP-based impurities, several protocols based on multiple heat treatments (sometimes under an NH_3 atmosphere) or repeated acid-/heat-treatments have

been developed [20, 21]. In this regard, Kramm et al. developed a novel purification method based on secondary heat-treatment under 10% H_2/N_2 gas (forming gas) followed by acid-leaching (Fig. 8a) [158]. As confirmed by Mössbauer spectroscopy, these purified Fe–N/C catalysts contained no particulate species and consisted exclusively of active Fe–N_x sites (Fig. 8b, c). This method was therefore suitable for the preparation of Fe–N/C catalysts with a high density of active sites (i.e., over 3 wt%). In addition, the ORR activity of the purified catalyst was enhanced 3–10 times in terms of the mass activity in acidic media, when compared to the catalyst that had not undergone secondary heat treatment (Fig. 8d). This strategy was found to be widely applicable to
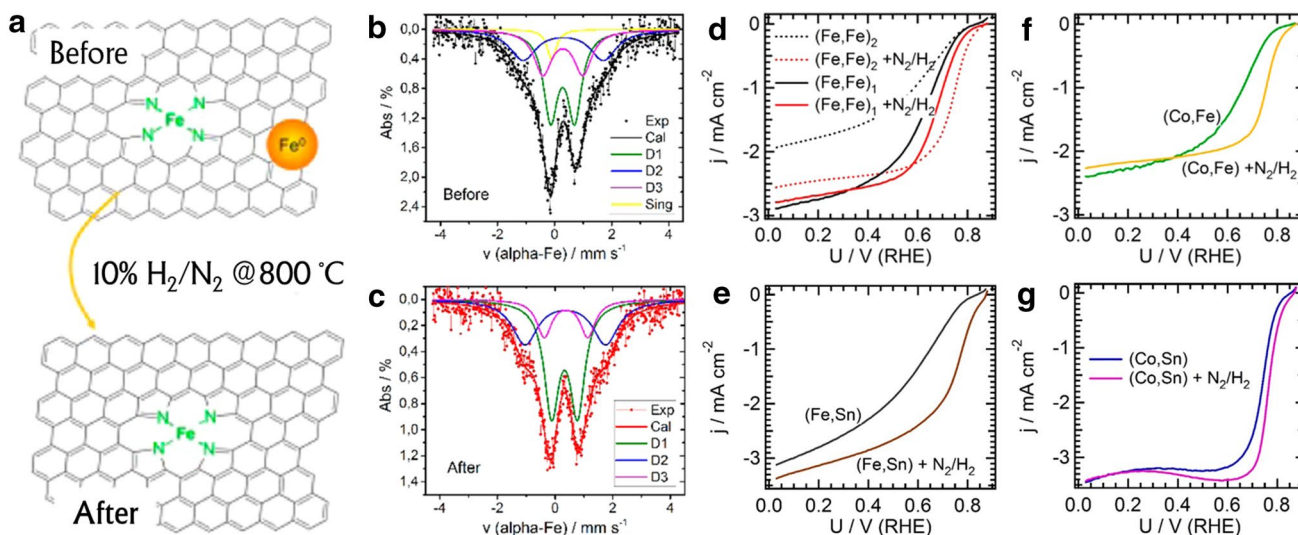
Fig. 8 a Schematic illustration of the catalyst purification process through heat-treatment under 10% H_2/N_2 (forming gas). Mössbauer spectra of the Fe–N/C catalysts, **b** before and **c** after purification. Signals D1–D3 represent structurally distinctive Fe–N_4 sites, while the Sing signal is attributed to the presence of superparamagnetic alpha-Fe. ORR polarization curves of the **d** Fe–N/C, **e** FeSn–N/C, **f** FeCo–N/C, and **g** CoSn–N/C catalysts before and after purification measured in 0.5 M H_2SO_4. Reproduced with permission from [158]. Copyright (2016) American Chemical Society

other metal-based M–N/C and bimetallic FeM–N/C catalysts (M = Co, Sn) (Fig. 8e–g) [158].

As an alternative strategy to preferentially generate M–N$_x$ active sites, Joo et al. developed the "silica-protectivel-layer-assisted" method to preserve Fe–N$_x$ sites during high-temperature pyrolysis [159]. For this process, 5,10,15,20-tetrakis(4-methoxyphenyl)porphine iron(III) chloride (Fe^{II}TMPPCl) was mixed with CNTs and annealed at 400 °C to allow the adsorption of FeTMPPCl on the CNT surfaces. A silica layer was then overcoated onto the CNT/FeTMPPCl composite using tetraethyl orthosilicate as the silica source. Pyrolysis and subsequent silica removal

resulted in a catalyst composed of a CNT coated with a thin porphyrinic carbon layer (CNT/PC) (Fig. 9a). The silica-coated CNT/PC was composed primarily of active Fe–N$_x$ sites, whereas the catalyst prepared without a silica over-coating (i.e., CNT/PC_w/o SiO$_2$) exhibited large Fe and Fe$_3$C NPs (Fig. 9b, c). Mössbauer spectroscopy and XAS revealed that the ratios of Fe–N$_x$ sites to Fe/Fe$_3$C species were approximately 3:1 and 1:1 for the CNT/PC and CNT/PC_w/o SiO$_2$ catalysts, respectively. In addition, temperature-controlled in situ XAS suggested the presence of interactions between the silica layer and the Fe–N$_4$ sites of FeTMPPCl, which could stabilize the Fe–N$_4$ sites and suppress

Fig. 9 a Schematic illustration of the "silica-protective-layer-assisted" strategy to preferentially generate Fe–N$_x$ active sites while suppressing the formation of Fe-based less-active particles. CNT/PC and CNT/PC_w/o SiO$_2$ denote the silica-protected and unprotected catalysts, respectively. TEM images of b CNT/PC and c CNT/PC_w/o SiO$_2$. ORR polarization curves of CNT/PC and CNT/PC_w/o SiO$_2$ measured in d 0.1 M KOH and e 0.1 M HClO$_4$. The insets show the kinetic current densities of the catalysts at 0.9 V (vs. RHE) in 0.1 M KOH and 0.8 V (vs. RHE) in 0.1 M HClO$_4$. Reproduced with permission from [159]. Copyright (2016) American Chemical Society
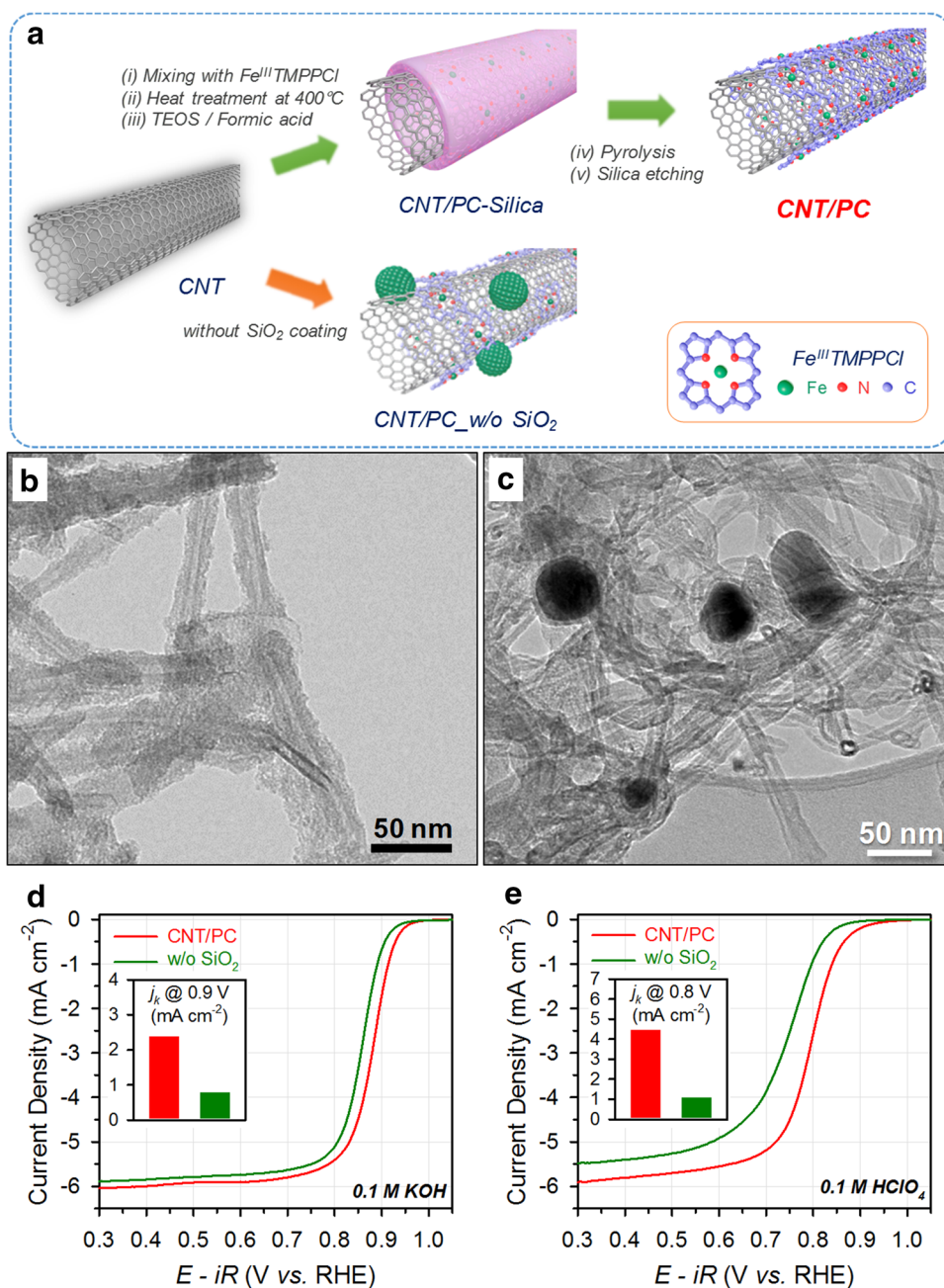
the formation of inactive Fe-based particles. The resulting CNT/PC catalyst exhibited high ORR activities with half-wave potentials of 0.88 and 0.79 V in 0.1 M KOH and 0.1 M HClO$_4$, respectively. CNT/PC catalyst prepared with the silica coating strategy exhibited 3–4 times higher ORR activities than the catalyst prepared with silica coating step both in acidic and alkaline electrolytes (Fig. 9d, e). When CNT/PC was employed as the cathode catalyst in MEA for an alkaline anion exchange membrane fuel cell (AEMFC), very high current density at 0.6 V and peak power density (i.e., 498 mA cm^{-2} and 380 mW cm^{-2}) were achieved, which were greater than those of previously reported AEMFC MEAs based on non-precious metal catalysts. The CNT/PC-based MEA also exhibited an excellent PEMFC performance with a volumetric activity of 320 A cm^{-3}, which compared favorably to the 2020 US DOE target of 300 A cm^{-3} [159]. Similarly, Zhang et al. prepared mesoporous silica-coated Co-doped ZIF-8 to prevent particle aggregation during pyrolysis [160]. In this case, the mesoporous silica shell performed dual roles during pyrolysis of the MOF precursor, i.e., prevention of Co-based particle formation and MOF particle fusion, leading to an increase in the BET surface area by a factor of two. These effects resulted in an enhancement in the ORR activity by approximately 6 times [160].

## 6 Non-pyrolyzed M–N/C Catalysts with Well-Defined Active Site Structures

The naturally occurring enzyme cytochrome c oxidase (CcO) is a key component in the respiratory cycle of organisms, selectively reducing oxygen molecules to H$_2$O without producing reactive oxygen species such as H$_2$O$_2$. The structure of CcO consists of a bimetallic center comprising an iron porphyrin with an axially coordinated histidine and a trihistidine-coordinated Cu in the distal pocket (Fig. 10a) [161]. Inspired by the elaborate structural features of CcO, significant of effort has been made to synthesize CcO-mimicking molecules, with the most successful example being

reported by the Collman group (Fig. 10b) [161]. Although such biomimetic molecules are useful in understanding the functions of CcO under physiologically relevant conditions (e.g., at pH ~ 7), they are unsuitable for PEMFC applications due to their instability under the harsh operating conditions required for PEMFCs, such as very low pH and working temperatures around 80 °C.

One would therefore expect that incorporation of the CcO-like structural moiety into heterogeneous electrocatalysts could in principle significantly boost their ORR activities. However, the high-temperature pyrolysis step commonly required for preparing heterogeneous ORR electrocatalysts would unavoidably cause the destruction and distortion of the M–N$_x$ sites [162–164]. Thus, as a compromise between molecular and heterogeneous catalysts, namely heterogenized molecular catalysts, have been developed by immobilizing CcO-mimicking molecules onto a conductive carbon support under ambient conditions, which can improve the stability of this moiety while preserving its catalytic functions.

A straightforward approach to the preparation of such catalysts involves the use of square planar M–N$_4$ structures, such as molecular phthalocyanines or porphyrins, which can be easily stabilized on carbon supports through π–π interactions [165–170]. For example, the Campidelli group reported the preparation of CNT–Co porphyrin layer core–sheath nanostructures [169]. They initially physisorbed designed Co porphyrin molecules onto CNT surfaces, then carried out polymerization to produce a porphyrin network layer on the CNTs (Fig. 11a). The resulting core–sheath catalyst exhibited an enhanced ORR activity compared to the catalyst bearing the physisorbed Co porphyrin. In this catalyst, the bifacial structure between the stacked layers of the Co porphyrin was suggested to be responsible for the near 4-electron selectivity, which is similar to the bimetallic interplay observed in CcO [161], in binuclear Cu-triazole–dipyridine complexes [170], and in bifacial Co-based porphyrins [171]. In addition, interaction of the Co-porphyrin units with the CNTs produced the catalysts with high stabilities in acidic

Fig. 10 **a** The active site of cytochrome c oxidase (CcO). The red, green, black, blue, and white spheres represent the Fe, Cu, N, O, and C atoms, respectively. **b** Synthetic analogue that has a similar structure and function to CcO. Reproduced with permission from [161]. Copyright (2007) American Association for the Advancement of Science
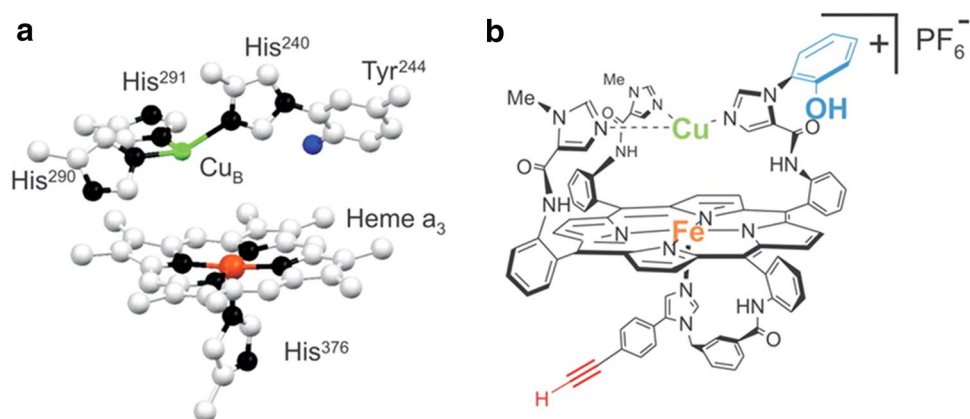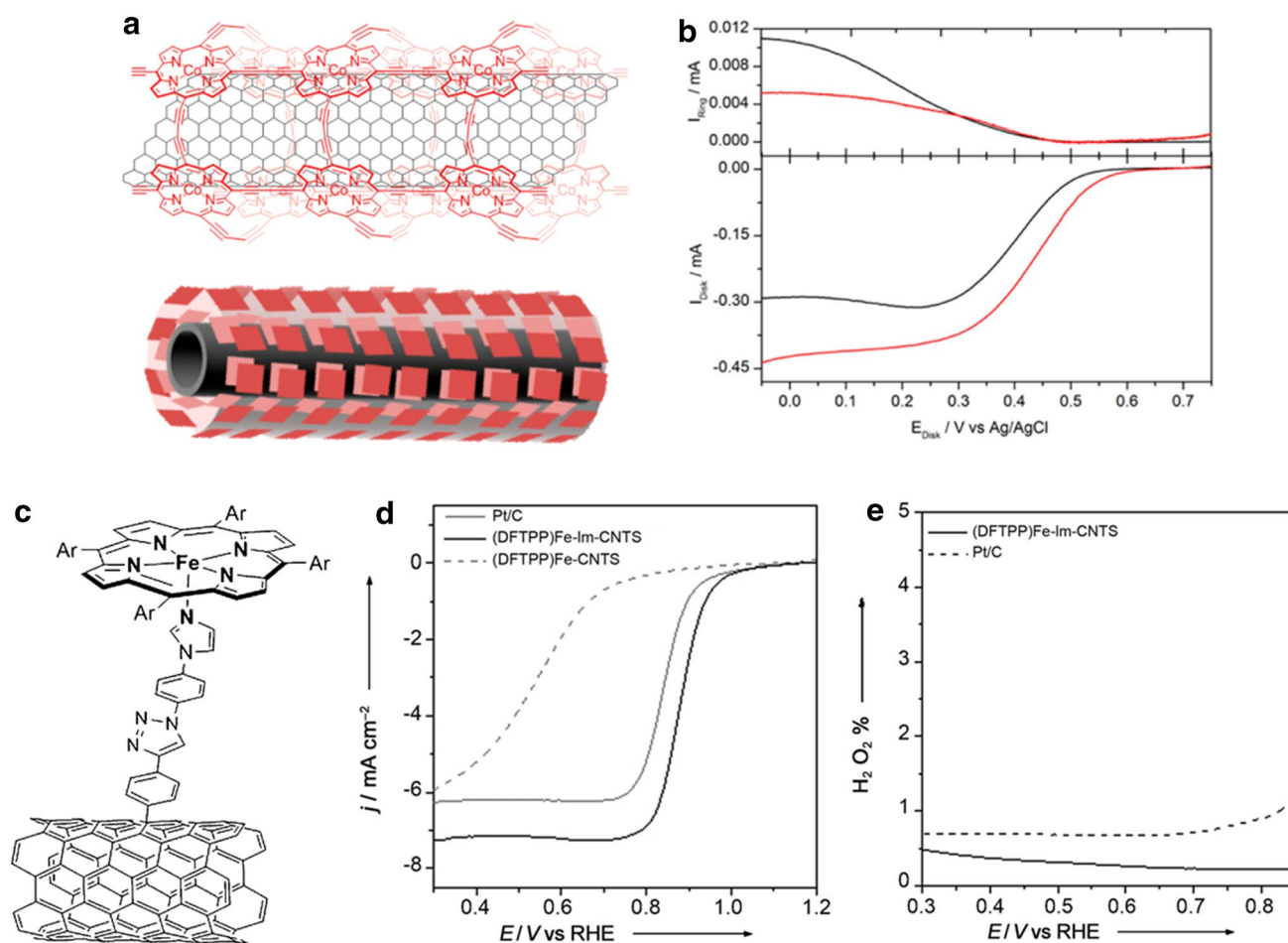
Fig. 11 **a** Schematic illustration of the polymeric Co porphyrin layers stacked on CNTs (MWNT–CoP). **b** ORR polarization curves of MWNT–CoP (red curve) and MWNT/CoP (black curve, physical mixture) measured in 0.5 M H_2SO_4. **c** Schematic representation of the heme-like active sites grafted onto a CNT through a coordination bond to the imidazolic N atom [(DFTPP)Fe-Im-CNTs]. **d** ORR polarization curves measured in 0.1 M $HClO_4$ and **e** electron transfer numbers during the ORR for (DFTPP)Fe-Im-CNTs and a simple physical mixture [(DFTPP)Fe-CNTs], measured using rotating ring disk electrode (RRDE). Reproduced with permission from [169]. Copyright (2014) American Chemical Society (a, b); Reproduced with permission from [173]. Copyright (2014) Wiley-VCH Verlag GmbH & Co. KGaA (c–e)

media, as confirmed by a minimal decrease in their ORR activities under such conditions [169].

Cho et al. developed a Fe–N/C catalyst with a biomimetic active center [172]. They covalently attached 4-aminopyridine onto a CNT surface, and anchored Fe^{II} phthalocyanine (FePc). The resulting heterogenized molecular catalyst exhibited a high activity, with a half-wave potential of 0.92 V (vs. RHE) and near 4-electron selectivity, which was superior to that of Pt/C in 0.1 M KOH. In this case, the strong coordination bond between the FePc molecule and pyridine formed a stable Fe–N$_4$–N$_{axial}$ active site structure, which is highly analogous to the structure of CcO. They suggested that Fe 3d rehybridization with the axial ligand orbital significantly modified the electronic structure of the Fe–N$_5$ sites compared to the square planar Fe–N$_4$ sites, thereby leading to increased ORR activity

through the facile cleavage of the O–O bond, as supported by DFT calculations [172].

Liu et al. also designed a bio-mimetic Fe–N$_5$ active site on a CNT surface [173], where they used an Fe porphyrin and an imidazolate axial ligand to enhance O_2 activation (Fig. 11c) [174, 175]. This catalyst exhibited the highest ORR activity among the previously reported non-pyrolytic M–N/C catalysts, with a half-wave potential of 0.88 V (vs. RHE) in an acidic solution (Fig. 11d). In addition, it was highly selective towards the 4-electron ORR (> 99.5% over the full potential range investigated, Fig. 11e) [173]. Although the Cho and the Liu groups demonstrated the high-performance of M–N/C catalysts through the use of heterogenized molecular catalysts, there is much room for improvement in the ORR activity/selectivity by tuning of

the macrocyclic molecules, ligand structures, and ligand-carbon support interactions.

The concept of "heterogenized molecular catalysts" based on low-temperature syntheses enables the identification of new active site structures for the ORR. Joo and Park et al. exploited the assembly of an archetypical organometallic compound, Co^{II} acetylacetonate [$Co(acac)_2$], with N-doped graphene to prepare a Co–N/C catalyst [176]. Simple stirring of a mixture of ammonia-reduced graphene oxide (A–rG–O) with $Co(acac)_2$ resulted in the formation of a hybrid catalyst (Co^{II}–A–rG–O). Solid-state nuclear magnetic resonance (SSNMR) measurements revealed that Co^{II}–A–rG–O contained alkyl groups, which were not detected for A–rG–O support, implying that the signal corresponding to the alkyl groups originated from the methyl groups of the $Co(acac)_2$ sites. This SSNMR result was supported by XAS observations, where the Co atoms in Co^{II}–A–rG–O exhibited similar spectral features to $Co(acac)_2$, with the exception of slightly elongated interatomic distances. In addition, density functional theory calculations suggested that the square planar $Co(acac)_2$ molecule has the highest affinity for bonding with the pyridinic N atoms in N-doped graphene. Based on these analyses, a novel type of active site was identified, namely the Co–O_4–N site, where Co ions are coordinated to four equatorial oxygen atoms from two acac ligands and to an axial N atom from A–rG–O (Fig. 12a). The creation of this

active site in Co^{II}–A–rG–O increased the onset potential by 90 mV compared to A–rG–O (Fig. 12b). In contrast, the increase in the ORR activity was negligible when $Co(acac)_2$ was added to N-free reflux-reduced graphene oxide (Re–G–O), highlighting the significance of Co–N coordination in the ORR. It was deduced that the Co–O_4–N site was responsible for promoting the 4-electron ORR, while the Co–O_4–O and Co–O_4–Ph (Ph = phenyl ring) species played an auxiliary role in peroxide reduction (Fig. 12d) [176]. It is noteworthy that the pentacoordinated Co–O_4–N sites resemble the geometric local structure of CcO.

7 Summary of the ORR Activities of Reported M–N/C Catalysts

The ORR activities of selected M–N/C catalysts measured in acidic and alkaline electrolytes are summarized in Tables 1 and 2, respectively. These tables provide the ORR activity parameters [i.e., half-wave potential, kinetic current density (j_k), and mass activity (j_m)], in addition to some selected experimental conditions, such as the electrolyte, catalyst loading, and type of counter electrode employed, all of which have a significant influence on the ORR activity.

It should be noted that the ORR activities of reported M–N/C catalysts are generally high in alkaline media,

Fig. 12 **a** Schematic description of ORR electrocatalysis on a Co–O_4–N active site. Polarization curves of **b** A–rG–O, Co^{II}–A–rG–O, and Pt/C and **c** Re–G–O, Co^{II}–Re–G–O, and Pt/C measured in 0.1 M KOH. **d** Electron transfer number for A–rG–O, Co^{II}–A–rG–O, Re–G–O, and Co^{II}–Re–G–O measured using the RRDE technique. Reproduced with permission from [176]. Copyright (2015) Wiley-VCH Verlag GmbH & Co. KGaA, Weinheim
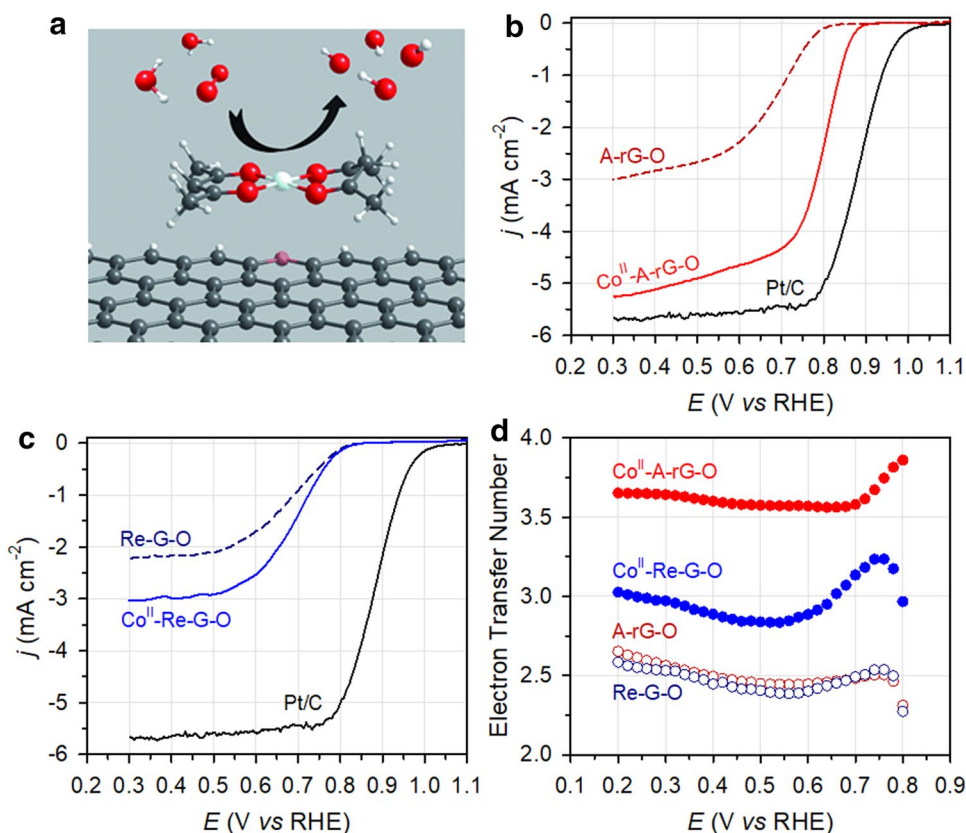
Table 1 Summary of the experimental conditions and the ORR activity parameters of reported M–N/C catalysts in acidic media

Catalysts	Electrolyte	Catalyst loading ($\mu g\ cm^{-2}$)	Counter electrode	Half-wave potential (V vs. RHE)[a]	j_k @ 0.8 V_{RHE} (mA cm^{-2})[b]	j_m @ 0.8 V_{RHE} (mA cm^{-2})[c]	References
PANI–FeCo–C	0.5 M H$_2$SO$_4$	600	Graphite rod	0.81	5.8	10	[21]
NT–G	0.1 M HClO$_4$	485	Graphite rod	0.76	2.1	4.3	[34]
Fe$_{0.5}$-950	0.1 M H$_2$SO$_4$	818	Graphite rod	0.89	> 100[d]	> 120[d]	[38]
FePhen@MOF-ArNH$_3$	0.1 M H$_2$SO$_4$	600	–	0.78	2.6	4.3	[39]
Fe/N/CF	0.5 M H$_2$SO$_4$	400	Au wire	0.80	6.3	16	[64]
FeIM/ZIF-8	0.1 M HClO$_4$	400	Au wire	0.76	2.6	6.5	[71]
C-FeZIF-900-0.84	0.1 M HClO$_4$	500	Pt wire	0.76	1.8	3.6	[75]
ZIF′-FA-CNT-p	0.1 M HClO$_4$	500	Pt wire	0.81	7.8	16	[76]
5% Fe–N/C	0.5 M H$_2$SO$_4$	260	Pt sheet	0.74	0.5	1.9	[78]
Fe-ISAs/CN	0.1 M HClO$_4$	408	Pt wire	0.77	1.9	4.7	[79]
Co–N–C	0.1 M HClO$_4$	600	Pt wire	0.76	1.1	1.8	[82]
ZIF-TAA-p	0.1 M HClO$_4$	500	Pt wire	0.77	1.6	3.2	[85]
LDH@ZIF-67-800	0.1 M HClO$_4$	200	Pt wire	0.68	0.3	1.5	[88]
Fe/N-gCB	0.05 M H$_2$SO$_4$	200	Pt wire	0.64	0.3	1.5	[99]
C-PANI/PBA	0.5 M H$_2$SO$_4$	360	Pt foil	0.69	0.4	1.1	[100]
CPM-99(Fe)/C	0.1 M HClO$_4$	600	Pt wire	0.73	0.7	1.2	[103]
PFeTMPP-1000	0.1 M HClO$_4$	400	Au wire	0.75	1.0	2.5	[106]
CoP-CMP800	0.5 M H$_2$SO$_4$	600	Pt wire	0.64	0.2	0.3	[108]
FeCo/C-800	0.1 M HClO$_4$	600	Pt wire	0.75	2.4	4.0	[109]
Fe3Mn–AAPyr	0.5 M H$_2$SO$_4$	600	Pt wire	0.75	0.8	1.3	[111]
Fe-8CBDZ	0.5 M H$_2$SO$_4$	600	Pt wire	0.78	2.0	3.3	[112]
FeCo-OMPC	0.1 M HClO$_4$	600	Pt wire	0.85	27	45	[117]
VB12/silica colloid	0.5 M H$_2$SO$_4$	600	Pt wire	0.79	3.5	5.8	[118]
Mesoporous Fe–N–C	0.1 M HClO$_4$	600	Pt	0.73	0.5	0.8	[121]
Fe-NMCSs	0.1 M HClO$_4$	255	Pt sheet	0.73	0.8	3.1	[127]
pCNT@Fe1.5@GL-NH$_3$	0.1 M HClO$_4$	600	Pt mesh	0.88	~ 100[d]	~ 170[d]	[135]
CPANI–Fe–NaCl	0.1 M HClO$_4$	600	Pt foil	0.73	0.7	1.2	[136]
Fe/Co-CMP-800	0.5 M H$_2$SO$_4$	600	Pt wire	0.78	2.5	4.2	[141]
Fe–N–C–3HT–2AL	0.1 M HClO$_4$	800	–	0.84	16.8	21	[143]
FeMo-C/N-3	0.5 M H$_2$SO$_4$	100	Pt wire	0.67	1.0	10	[144]
S/N_Fe$_{27}$	0.1 M HClO$_4$	800	Pt gauze	0.83	13.4	17	[151]
Fe/N/C-SCN	0.1 M H$_2$SO$_4$	600	GC plate	0.84	13.8	23	[152]
AT-Fe/N/C	0.1 M H$_2$SO$_4$	600	Graphite plate	0.81	5.4	9	[153]
(Fe, Fe)$_2$ + N$_2$/H$_2$	0.5 M H$_2$SO$_4$	130	Pt wire	0.73	0.4	3.1	[158]
CNT/PC	0.1 M HClO$_4$	800	Graphite	0.79	4.5	5.6	[159]
Co, N-CNF	0.5 M H$_2$SO$_4$	360	Pt wire	0.67	–	–	[160]
Co corrole/BP2000	0.5 M H$_2$SO$_4$	400	GC rod	0.73	1.3	3.2	[167]
MWNT-CoP **1**	0.5 M H$_2$SO$_4$	155	Graphite plate	0.66	0.2	1.3	[169]
FePc-Py-CNT	0.5 M H$_2$SO$_4$	318	Pt wire	0.66	0.4	1.3	[172]
(DFTPP)Fe-Im-CNTs	0.1 M HClO$_4$	1000	Graphite rod	0.88	~ 50[d]	~ 50[d]	[173]
Fe–N/C-800	0.1 M HClO$_4$	100	Pt	0.66	0.1	1.0	[179]
PpPD–Fe–C	0.5 M H$_2$SO$_4$	900	Graphite rod	0.72	0.5	0.6	[180]
Fe$_3$C/NG-800	0.1 M HClO$_4$	400	Pt foil	0.77	0.8	2.0	[181]
Fe-PANI + DCDA	0.5 M H$_2$SO$_4$	1000	Graphite rod	0.83	8.6	8.6	[185]
Fe–N–C–Phen–PANI	0.5 M H$_2$SO$_4$	600	Graphitic electrode	0.80	3.4	5.7	[186]

[a]The half-wave potential was determined to be the potential where the measured current (j) was equal to $0.5 \times j_d$ (j_d: diffusion limited current density). In some cases, j_d is not well developed in plateau-shape, and thus was assumed to be j at 0.2–0.4 V (vs. RHE)

[b]Kinetic current density at 0.8 V (vs. RHE), calculated using the following equation: $j_k = j \times j_d/(j_d − j)$, where j_d was assumed to be j at 0.2–0.4 V (vs. RHE)

[c]Mass activity at 0.8 V (vs. RHE). $j_m = j_k/$(catalyst loading, mg cm^{-2})

[d]j_k values were estimated from extrapolation of the Tafel line, as the measured current density was too close to the j_d value

Table 2 Summary of the experimental conditions and the ORR activity parameters of reported M–N/C catalysts in alkaline media

Catalysts	Electrolyte	Catalyst loading ($\mu g\ cm^{-2}$)	Counter electrode	Half-wave potential (V vs. RHE)[a]	j_k @ 0.9 V_{RHE} ($mA\ cm^{-2}$)[b]	j_m @ 0.9 V_{RHE} ($mA\ cm^{-2}$)[c]	References
NT–G	0.1 M KOH	485	Graphite rod	0.88	2.9	6.0	[34]
FePhen@MOF-ArNH3	0.1 M KOH	600	–	0.86	1.9	3.2	[39]
Co_9S_8@CNS900	0.1 M KOH	400	Pt foil	0.80	0.1	0.2	[70]
NCNTs-20	0.1 M KOH	570	Pt foil	0.83	1.2	2.1	[72]
C-FeZIF-900-0.84	0.1 M KOH	500	Pt wire	0.84	1.2	2.4	[75]
Fe-ISAs/CN	0.1 M KOH	408	Pt wire	0.90	6.06	15	[79]
Co–N–C	0.1 M KOH	283	Pt wire	0.87	1.2	4.2	[82]
ZIF-TAA-p	0.1 M KOH	500	Pt wire	0.88	1.8	3.6	[85]
LDH@ZIF-67-800	0.1 M KOH	200	Pt wire	0.83	0.2	1.0	[88]
Co_4N/CNW/CC-A	1 M KOH	–	Graphite plate	0.85	4.3	–	[89]
Co SAs/N-C(900)	0.1 M KOH	408	Pt wire	0.88	2.0	4.9	[90]
Co/NC	0.1 M KOH	210	Pt wire	0.83	0.3	1.4	[91]
Cal-CoZIF-VXC72-H	0.1 M KOH	408	Pt foil	0.86	0.7	1.7	[92]
N-CNTs-650	0.1 M KOH	–	Pt wire	0.85	0.3	–	[96]
Fe/N-gCB	0.1 M KOH	200	Pt wire	0.83	0.9	4.5	[99]
C-PANI/PBA	0.1 M KOH	360	Pt foil	0.85	1.3	3.6	[100]
CPM-99(Fe)/C	0.1 M KOH	200	Pt wire	0.80	0.3	1.5	[103]
Cu-NC-Air	0.1 M KOH	300	Pt wire	0.83	0.6	2.0	[105]
FeCo/C-800	0.1 M KOH	200	Pt wire	0.85	1.1	5.5	[109]
FeCo-OMPC	0.1 M KOH	300	Pt wire	0.86	1.8	6.0	[117]
Mesoporous Fe–N–C	0.1 M KOH	200	Pt	0.84	0.8	4.0	[121]
Fe-N/C-800	0.1 M KOH	79.6	Pt wire	0.81	0.6	7.5	[126]
Fe-NMCSs	0.1 M KOH	255	Pt sheet	0.86	1.7	6.7	[127]
Fe-N-SCCFs	0.1 M KOH	600	Graphite rod	0.88	3.7	6.2	[130]
MF-Fe-800	0.1 M KOH	200	Pt coil	0.83	0.63	3.2	[133]
$Co_{0.05}$,N_pCNT	0.1 M KOH	200	Pt mesh	0.87	3.2	16	[134]
pCNT@Fe1.5@GL	0.1 M KOH	200	Pt mesh	0.87	2.3	12	[135]
Fe/Fe_3C@N-C-NaCl	0.1 M KOH	600	Pt wire	0.87	1.7	2.8	[138]
CS-FePc_450	0.1 M KOH	274	Pt wire	0.88	2.5	9.1	[139]
(Fe,Mn)–N–C–3HT–2AL	0.1 M KOH	800	–	0.90	5.6	7.0	[143]
N-GCNT/FeCo-3	0.1 M KOH	200	Pt foil	0.92	7.8	39	[145]
Fe/ANT/C	0.1 M KOH	600	Pt foil	0.86	1.7	2.8	[150]
S/N_Fe_{27}	0.1 M KOH	800	Pt gauze	0.87	3.1	3.9	[151]
AT-Fe/N/C	0.1 M NaOH	600	Graphite plate	0.93	~20	~33	[153]
CNT/PC	0.1 M KOH	800	Graphite rod	0.88	2.4	3.0	[159]
Co,N-CNF	0.1 M KOH	120	Pt wire	0.81	0.1	0.8	[160]
FePc-Py-CNT	0.1 M KOH	318	Pt wire	0.92	8.7	27	[172]
(DFTPP)Fe-Im-CNTs	0.1 M KOH	1000	Graphite rod	0.92	12	12	[173]
Co^{II}–A–rG–O	0.1 M KOH	600	Graphite rod	0.81	<0.1	0.1	[176]
N-Fe-CNT/CNP	0.1 M NaOH	1000	Graphite rod	0.93	7.2	7.2	[177]
Fe-PyNG	0.1 M KOH	140	Pt sheet	0.81	0.7	5.0	[178]
Fe–N/C-800	0.1 M KOH	100	Pt	0.81	0.9	9.0	[179]
Fe_3C/NG-800	0.1 M KOH	400	Pt foil	0.86	1.6	4.0	[181]
Cu-N@C-60	0.1 M KOH	298.6	Graphite rod	0.79	0.1	0.3	[182]
Fe@C-FeNC-2	0.1 M KOH	700	–	0.90	5.1	7.3	[183]
Fe_3C@N-CNT	0.1 M KOH	250	Pt plate	0.85	1.2	4.8	[184]
Fe-PANI+DCDA	0.1 M NaOH	1000	Graphite rod	0.91	6.3	6.3	[185]

[a]The half-wave potential was determined to be the potential where the measured current (j) was equal to $0.5 \times j_d$ (j_d: diffusion limited current density). In some cases, j_d is not well developed in plateau-shape, and thus was assumed to be j at 0.2–0.4 V (vs. RHE)

[b]Kinetic current density at 0.9 V (vs. RHE), calculated using the following equation: $j_k = j \times j_d/(j_d - j)$, where j_d was assumed to be j at 0.2–0.4 V (vs. RHE)

[c]Mass activity at 0.9 V (vs. RHE). $j_m = j_k/$(catalyst loading, $mg\ cm^{-2}$)
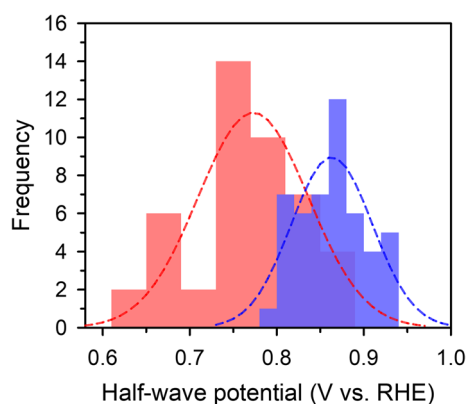
Fig. 13 Histogram of the half-wave potentials of previously reported M–N/C catalysts measured in acidic (indicated as red bars) and in alkaline media (indicated as blue bars). Detailed ORR activity parameters of the examined catalysts are summarized in Tables 1 and 2

with the majority of catalysts exhibiting half-wave potentials > 0.8 V, and on average ~ 0.85 V (vs. RHE). In acidic electrolytes, however, the catalysts show ~ 100 mV lower half-wave potentials (Fig. 13). Recently, it was found that this decline in the ORR activities of these catalysts in acidic media coincides with the protonation of pyridinic N sites, which may provide a clue to such a discrepancy [187]. However, the mechanism responsible for the differences in ORR activities between acidic and alkaline media remains unclear, and requires further systematic studies.

Finally, we note that the majority of research groups (> 60% of the literature examined) employ Pt-based counter electrodes in their studies. However, the platinum is prone to be anodically dissolved, and can be redeposited on the nonprecious catalyst layer, leading to an enhancement in the ORR activity. Such an effect would become more apparent in long-term durability/stability tests. Indeed, the activation behavior caused by the Pt dissolution–redeposition process has recently been investigated in the context of electrocatalytic hydrogen evolution [188, 189]. The accidental incorporation of Pt prevents a fair comparison of the ORR activity, and therefore the use of carbon-based materials as the counter electrode is highly recommended.

8 Conclusions and Outlook

This review presented the recently emerged synthetic strategies toward high-performance M–N/C catalysts for the ORR, and summarized the ORR activities of highly active M–N/C catalysts. While many methods have been developed, we identified five major strategies for enhancing the catalytic activity for the ORR: the exploitation of MOFs as hosts or precursors, the use of sacrificial templates, the addition of heteroelements, the preferential generation of active sites,

and a biomimetic approach. We summarized the advantages of each preparation method for M–N/C catalysts and presented representative examples for each strategy.

The advances in the preparation of M–N/C catalysts, along with the progress in the identification of their active sites for the ORR, indeed led to highly active catalysts, with some catalysts showing very high ORR activities that can rival that of a Pt/C catalyst. However, such performances are in most cases attained with the rotating disk electrode (RDE) measurements in a half-cell configuration [190]. Compared to the RDE measurements, only limited examples of MEA-based single cell performances have been reported. Furthermore, it is often the case that excellent RDE performances of M–N/C catalysts are not fully translated in MEA measurements. Hence, to realize M–N/C catalysts as a true alternative to the state-of-the-art Pt/C catalyst, the performance improvement of MEAs based on M–N/C catalysts is essential. In this sense, very recent result of the Zelenay group [45], who demonstrated highly promising MEA performances for H$_2$-air PEMFC employing a newly developed Fe–N/C catalyst, sheds light on the practicality of this class of catalysts into the fuel cell market.

References

1. Bockris JOM (2002) The origin of ideas on a hydrogen economy and its solution to the decay of the environment. Int J Hydrog Energy 27:731–740
2. Chu S, Majumdar A (2012) Opportunities and challenges for a sustainable energy future. Nature 488:294–303
3. Turner JA (2004) Sustainable hydrogen production. Science 305:972–974
4. Park S, Shao Y, Liu J, Wang Y (2012) Oxygen electrocatalysts for water electrolyzers and reversible fuel cells: status and perspective. Energy Environ Sci 5:9331–9344
5. Katsounaros I, Cherevko S, Zeradjanin AR, Mayrhofer KJJ (2014) Oxygen electrochemistry as a cornerstone for sustainable energy conversion. Angew Chem Int Ed 53:102–121
6. Chu S, Cui Y, Liu N (2017) The path towards sustainable energy. Nat Mater 16:16–22
7. Seh ZW, Kibsgaard J, Dickens CF, Chorkendorff I, Nørskov JK, Jaramillo TF (2017) Combining theory and experiment in electrocatalysis: insights into materials design. Science 355:eaad4998
8. Wang Y, Chen KS, Mishler J, Cho SC, Adroher XC (2011) A review of polymer electrolyte membrane fuel cells: technology, applications, and needs on fundamental research. Appl Energy 88:981–1007

9. Debe MK (2012) Electrocatalyst approaches and challenges for automotive fuel cells. Nature 486:43–51

10. Vielstich W, Lamm A, Gasteiger HA (2003) Handbook of fuel cells: vol 2: fundamentals, technology, applications. Wiley, New York

11. Gasteiger HA, Kocha SS, Sompalli B, Wagner FT (2005) Activity benchmark and requirements for Pt, Pt-alloy, and non-Pt oxygen reduction catalysts for PEMFCs. Appl Catal B 56:9–35

12. Papageorgopoulos D (2016) U.S. DOE Hydrogen and Fuel Cells Program 2016 Annual Review Meeting. https://www.hydrogen.energy.gov/pdfs/review16/fc000_papageorgopoulos_2016_o.pdf. Accessed 11 Aug 2017

13. Liang Y, Li Y, Wang H, Dai H (2013) Strongly coupled inorganic/nanocarbon hybrid materials for advanced electrocatalysis. J Am Chem Soc 135:2013–2036

14. Wu ZS, Yang S, Sun Y, Parvez K, Feng X, Müllen K (2012) 3D nitrogen-doped graphene aerogel-supported Fe_3O_4 nanoparticles as efficient electrocatalysts for the oxygen reduction reaction. J Am Chem Soc 134:9082–9085

15. Ling T, Yan DY, Jiao Y, Wang H, Zheng Y, Zheng X, Mao J, Du XW, Hu Z, Jaroniec M, Qiao SZ (2016) Engineering surface atomic structure of single-crystal cobalt (II) oxide nanorods for superior electrocatalysis. Nat Commun 7:12876

16. Gao MR, Jiang J, Yu SH (2012) Solution-based synthesis and design of late transition metal chalcogenide materials for oxygen reduction reaction (ORR). Small 8:13–27

17. Deng D, Yu L, Chen X, Wang G, Jin L, Pan X, Deng J, Sun G, Bao X (2013) Iron encapsulated within pod-like carbon nanotubes for oxygen reduction reaction. Angew Chem Int Ed 52:371–375

18. Hu Y, Jensen JO, Zhang W, Cleemann LN, Xing W, Bjerrum NJ, Li Q (2014) Hollow spheres of iron carbide nanoparticles encased in graphitic layers as oxygen reduction catalysts. Angew Chem Int Ed 53:3675–3679

19. Jaouen F, Herranz J, Lefèvre M, Dodelet JP, Kramm UI, Herrmann I, Bogdanoff P, Maruyama J, Nagaoka T, Garsuch A, Dahn JR, Olson T, Pylypenko S, Atanassov P, Ustinov EA (2009) Cross-laboratory experimental study of non-noble-metal electrocatalysts for the oxygen reduction reaction. ACS Appl Mater Interfaces 1:1623–1639

20. Lefèvre M, Proietti E, Jaouen F, Dodelet JP (2009) Iron-based catalysts with improved oxygen reduction activity in polymer electrolyte fuel cells. Science 324:71–74

21. Wu G, More KL, Johnston CM, Zelenay P (2011) High-performance electrocatalysts for oxygen reduction derived from polyaniline, iron, and cobalt. Science 332:443–447

22. Bayatsarmadi B, Zheng Y, Vasileff A, Qiao SZ (2017) Recent advances in atomic metal doping of carbon-based nanomaterials for energy conversion. Small 13:1700191

23. Zhu YP, Guo C, Zheng Y, Qiao SZ (2017) Surface and interface engineering of noble-metal-free electrocatalysts for efficient energy conversion processes. Acc Chem Res 50:915–923

24. Gong K, Du F, Xia Z, Durstock M, Dai L (2009) Nitrogen-doped carbon nanotube arrays with high electrocatalytic activity for oxygen reduction. Science 323:760–764

25. Zheng Y, Jiao Y, Jaroniec M, Jin Y, Qiao SZ (2012) Nanostructured metal-free electrochemical catalysts for highly efficient oxygen reduction. Small 8:3550–3566

26. Jasinski R (1964) A new fuel cell cathode catalyst. Nature 201:1212–1213

27. Alt H, Binder H, Sandstede G (1973) Mechanism of the electrocatalytic reduction of oxygen on metal chelates. J Catal 28:8–19

28. Randin JP (1974) Interpretation of the relative electrochemical activity of various metal phthalocyanines for the oxygen reduction reaction. Electrochim Acta 19:83–85

29. Jahnke H, Schönborn M, Zimmermann G (1976) Organic dye-stuffs as catalysts for fuel cells. Top Curr Chem 61:133–181

30. Gupta S, Tryk D, Bae I, Aldred W, Yeager E (1989) Heat-treated polyacrylonitrile-based catalysts for oxygen electroreduction. J Appl Electrochem 19:19–27

31. Schulenburg H, Stankov S, Schünemann V, Radnik J, Dorbandt I, Fiechter S, Bogdanoff P, Tributsch H (2003) Catalysts for the oxygen reduction from heat-treated iron(III) tetramethoxyphenyl-porphyrin chloride: structure and stability of active sites. J Phys Chem B 107:9034–9041

32. Koslowski UI, Abs-Wurmbach I, Fiechter S, Bogdanoff P (2008) Nature of the catalytic centers of porphyrin-based electrocatalysts for the ORR: a correlation of kinetic current density with the site density of Fe–N_4 centers. J Phys Chem C 112:15356–15366

33. Kramm UI, Herranz J, Larouche N, Arruda TM, Lefèvre M, Jaouen F, Bogdanoff P, Fiechter S, Abs-Wurmbach I, Mukerjee S, Dodelet JP (2012) Structure of the catalytic sites in Fe/N/C-catalysts for O_2-reduction in PEM fuel cells. Phys Chem Chem Phys 14:11673–11688

34. Li Y, Zhou W, Wang H, Xie L, Liang Y, Wei F, Idrobo JC, Pennycook SJ, Dai H (2012) An oxygen reduction electrocatalyst based on carbon nanotube–graphene complexes. Nat Nanotechnol 7:394–400

35. Oberst JL, Thorum MS, Gewirth AA (2012) Effect of pH and azide on the oxygen reduction reaction with a pyrolyzed Fe phthalocyanine catalyst. J Phys Chem C 116:25257–25261

36. Tylus U, Jia Q, Strickland K, Ramaswamy N, Serov A, Atanassov P, Mukerjee S (2014) Elucidating oxygen reduction active sites in pyrolyzed metal–nitrogen coordinated non-precious-metal electrocatalyst systems. J Phys Chem C 118:8999–9008

37. Kramm UI, Lefèvre M, Larouche N, Schmeisser D, Dodelet JP (2014) Correlations between mass activity and physicochemical properties of Fe/N/C catalysts for the ORR in PEM fuel cell via ^{57}Fe Mössbauer spectroscopy and other techniques. J Am Chem Soc 136:978–985

38. Zitolo A, Goellner V, Armel V, Sougrati MT, Mineva T, Stievano L, Fonda E, Jaouen F (2015) Identification of catalytic sites for oxygen reduction in iron- and nitrogen-doped graphene materials. Nat Mater 14:937–942

39. Strickland K, Miner E, Jia Q, Tylus U, Ramaswamy N, Liang W, Sougrati MT, Jaouen F, Mukerjee S (2015) Highly active oxygen reduction non-platinum group metal electrocatalyst without direct metal–nitrogen coordination. Nat Commun 6:7343

40. Malko D, Kucernak A, Lopes T (2016) In situ electrochemical quantification of active sites in Fe–N/C non-precious metal catalysts. Nat Commun 7:13285

41. Kim JH, Sa YJ, Jeong HY, Joo SH (2017) Roles of Fe–N_x and Fe–Fe_3C@C species in Fe–N/C electrocatalysts for oxygen reduction reaction. ACS Appl Mater Interfaces 9:9567–9575

42. Zheng Y, Jiao Y, Zhu Y, Cai Q, Vasileff A, Li LH, Han Y, Chen Y, Qiao SZ (2017) Molecular-level g-C_3N_4 coordinated transition metals as a new class of electrocatalysts for oxygen electrode reactions. J Am Chem Soc 139:3336–3339

43. Yang XD, Zheng Y, Yang J, Shi W, Zhong JH, Zhang C, Zhang X, Hong YH, Peng XX, Zhou ZY, Sun SG (2017) Modeling Fe/N/C catalysts in monolayer graphene. ACS Catal 7:139–145

44. Wu KH, Shi W, Wang D, Xu J, Ding Y, Lin Y, Qi W, Zhang B, Su D (2017) In situ electrostatic modulation of path selectivity for the oxygen reduction reaction on Fe–N doped carbon catalyst. Chem Mater 29:4649–4653

45. Chung HT, Cullen DA, Higgins D, Sneed BT, Holby EF, More KL, Zelenay P (2017) Direct atomic-level insight into the active sites of a high-performance PGM-free ORR catalyst. Science 357:479–484

46. Bezerra CWB, Zhang L, Lee K, Liu H, Marques ALB, Marques EP, Wang H, Zhang J (2008) A review of Fe–N/C and Co–N/C

catalysts for the oxygen reduction reaction. Electrochim Acta 53:4937–4951

47. Jaouen F, Proietti E, Lefèvre M, Chenitz R, Dodelet JP, Wu G, Chung HT, Johnston CM, Zelenay P (2011) Recent advances in non-precious metal catalysis for oxygen-reduction reaction in polymer electrolyte fuel cells. Energy Enrivon Sci 4:114–130

48. Morozan A, Jousselme B, Palacin S (2011) Low-platinum and platinum-free catalysts for the oxygen reduction reaction at fuel cell cathodes. Energy Enrivon Sci 4:1238–1254

49. Chen Z, Higgins D, Yu A, Zhang L, Zhang J (2011) A review on non-precious metal electrocatalysts for PEM fuel cells. Energy Enrivon Sci 4:3167–3192

50. Zagal JH, Koper MTM (2016) Reactivity descriptors for the activity of molecular MN4 catalysts for the oxygen reduction reaction. Angew Chem Int Ed 55:14510–14521

51. Jia Q, Ramaswamy N, Tylus U, Strickland K, Li J, Serov A, Artyushkova K, Atanassov P, Anibal J, Gumeci C, Barton SC, Sougrati MT, Jaouen F, Halevi B, Mukerjee S (2016) Spectroscopic insights into the nature of active sites in iron–nitrogen–carbon electrocatalysts for oxygen reduction in acid. Nano Energy 29:65–82

52. Sa YJ, Kim JH, Joo SH (2017) Recent progress in the identification of active sites in pyrolyzed Fe–N/C catalysts and insights into their role in oxygen reduction reaction. J Electrochem Sci Technol 8(3):169–182

53. Masa J, Xia W, Muhler M, Schuhmann W (2015) On the role of metals in nitrogen-doped carbon electrocatalysts for oxygen reduction. Angew Chem Int Ed 54:10102–10120

54. Shen M, Wei C, Ai K, Lu L (2017) Transition metal–nitrogen–carbon nanostructured catalysts for the oxygen reduction reaction: from mechanistic insights to structural optimization. Nano Res 10:1449–1470

55. Dombrovskis JK, Palmqvist AEC (2016) Recent progress in synthesis, characterization and evaluation of non-precious metal catalysts for the oxygen reduction reaction. Fuel Cells 16:4–22

56. Shao M, Chang Q, Dodelet JP, Chenitz R (2016) Recent advances in electrocatalysts for oxygen reduction reaction. Chem Rev 116:3594–3657

57. Yaghi OM, O'Keeffe M, Ockwig NW, Chae HK, Eddaoudi M, Kim J (2003) Reticular synthesis and the design of new materials. Nature 423:705–714

58. Cordova KE, O'Keeffe M, Yaghi OM (2013) The chemistry and applications of metal-organic frameworks. Science 341:1230444

59. Liu J, Zhu D, Guo C, Vasileff A, Qiao SZ (2017) Design strategies toward advanced MOF-derived electrocatalysts for energy-conversion reactions. Adv Energy Mater 7:1700518

60. Proietti E, Jaouen F, Lefèvre M, Larouche N, Tian J, Herranz J, Dodelet JP (2011) Iron-based cathode catalyst with enhanced power density in polymer electrolyte membrane fuel cells. Nat Commun 2:416

61. Palaniselvam T, Biswal BP, Banerjee R, Kurungot S (2013) Zeolitic imidazolate framework (ZIF)-derived, hollow-core, nitrogen-doped carbon nanostructures for oxygen-reduction reactions in PEFCs. Chem Eur J 19:9335–9342

62. Zhao D, Shui JL, Grabstanowicz LR, Chen C, Commet SM, Xu T, Lu J, Liu DJ (2014) Highly efficient non-precious metal electrocatalysts prepared from one-pot synthesized zeolitic imidazolate frameworks. Adv Mater 26:1093–1097

63. Armel V, Hindocha S, Salles F, Bennett S, Jones D, Jaouen F (2017) Structural descriptors of zeolitic–imidazolate frameworks are keys to the activity of Fe–N–C catalysts. J Am Chem Soc 139:453–464

64. Shui J, Chen C, Grabstanowicz L, Zhao D, Liu DJ (2015) Highly efficient nonprecious metal catalyst prepared with metal–organic framework in a continuous carbon nanofibrous network. Proc Natl Acad Sci 112:10629–10634

65. Sun H, Su H, Ma X, Zhang P, Zhang X, Dai X, Gao J, Chen C, Sun SG (2016) Fe/IRMOF-3 derived porous carbons as non-precious metal electrocatalysts with high activity and stability towards oxygen reduction reaction. Electrochim Acta 205:53–61

66. Bhattacharyya S, Konkena B, Jayaramulu K, Schuhmann W, Maji TK (2017) Synthesis of nano-porous carbon and nitrogen doped carbon dots from an anionic MOF: a trace cobalt metal residue in carbon dots promotes electrocatalytic ORR activity. J Mater Chem A 5:13573–13580

67. Huang X, Yang Z, Dong B, Wang Y, Tang T, Hou Y (2017) In situ Fe$_2$N@N-doped porous carbon hybrids as superior catalysts for oxygen reduction reaction. Nanoscale 9:8102–8106

68. Zhao S, Yin H, Du L, He L, Zhao K, Chang L, Yin G, Zhao H, Liu S, Tang Z (2014) Carbonized nanoscale metal–organic frameworks as high performance electrocatalyst for oxygen reduction reaction. ACS Nano 8:12660–12668

69. Li JS, Li SL, Tang YJ, Han M, Dai ZH, Bao JC, Lan YQ (2015) Nitrogen-doped Fe/Fe$_3$C@graphitic layer/carbon nanotube hybrids derived from MOFs: efficient bifunctional electrocatalysts for ORR and OER. Chem Commun 51:2710–2713

70. Zhu QL, Xia W, Akita T, Zou R, Xu Q (2016) Metal-organic framework-derived honeycomb-like open porous nanostructures as precious-metal-free catalysts for highly efficient oxygen electroreduction. Adv Mater 28:6391–6398

71. Zhao D, Shui JL, Chen C, Chen X, Reprogle BM, Wang D, Liu DJ (2012) Iron imidazolate framework as precursor for electrocatalysts in polymer electrolyte membrane fuel cells. Chem Sci 3:3200–3205

72. Su P, Xiao H, Zhao J, Yao Y, Shao Z, Li C, Yang Q (2013) Nitrogen-doped carbon nanotubes derived from Zn–Fe-ZIF nanospheres and their application as efficient oxygen reduction electrocatalysts with in situ generated iron species. Chem Sci 4:2941–2946

73. Liu T, Zhao P, Hua X, Luo W, Chen S, Cheng G (2016) An Fe–N–C hybrid electrocatalyst derived from a bimetal–organic framework for efficient oxygen reduction. J Mater Chem A 4:11357–11364

74. Li Z, Sun H, Wei L, Jiang WJ, Wu M, Hu JS (2017) Lamellar metal organic framework-derived Fe–N–C non-noble electrocatalysts with bimodal porosity for efficient oxygen reduction. ACS Appl Mater Interfaces 9:5272–5278

75. Deng Y, Dong Y, Wang G, Sun K, Shi X, Zheng L, Li X, Liao S (2017) Well-defined ZIF-derived Fe–N codoped nanoframes as efficient oxygen reduction catalysts. ACS Appl Mater Interfaces 9:9699–9709

76. Zhang C, Wang YC, An B, Huang R, Wang C, Zhou Z, Lin W (2017) Networking pyrolyzed zeolitic imidazolate frameworks by carbon nanotubes improves conductivity and enhances oxygen-reduction performance in polymer-electrolyte-membrane fuel cells. Adv Mater 29:1604556

77. Pei Y, Qi Z, Li X, Maligal-Ganesh RV, Goh TW, Xiao C, Wang T, Huang W (2017) Morphology inherence from hollow MOFs to hollow carbon polyhedrons in preparing carbon-based electrocatalysts. J Mater Chem A 5:6186–6192

78. Lai Q, Zheng L, Liang Y, He J, Zhao J, Chen J (2017) Metal–organic-framework-derived Fe-N/C electrocatalyst with five-coordinated Fe-N$_x$ sites for advanced oxygen reduction in acid media. ACS Catal 7:1655–1663

79. Chen Y, Ji S, Wang Y, Dong J, Chen W, Li Z, Shen R, Zheng L, Zhuang Z, Wang D, Li Y (2017) Isolated single iron atoms anchored on N-doped porous carbon as an efficient electrocatalyst for the oxygen reduction reaction. Angew Chem Int Ed 56:6937–6941

80. Goenaga G, Ma S, Yuan S, Liu DJ (2010) New approaches to non-PGM electrocatalysts using porous framework materials. ECS Trans 33:579–586

81. Ma S, Goenaga GA, Call AV, Liu DJ (2011) Cobalt imidazolate framework as precursor for oxygen reduction reaction electrocatalysts. Chem Eur J 17:2063–2067

82. You B, Jiang N, Sheng M, Drisdell WS, Yano J, Sun Y (2015) Bimetal–organic framework self-adjusted synthesis of support-free nonprecious electrocatalysts for efficient oxygen reduction. ACS Catal 5:7068–7076

83. Hou Y, Wen Z, Cui S, Ci S, Mao S, Chen J (2015) An advanced nitrogen-doped graphene/cobalt-embedded porous carbon polyhedron hybrid for efficient catalysis of oxygen reduction and water splitting. Adv Funct Mater 25:872–882

84. Chen YZ, Wang C, Wu ZY, Xiong Y, Wu Q, Yu SH, Jiang HL (2015) From bimetallic metal-organic framework to porous carbon: high surface area and multicomponent active dopants for excellent electrocatalysis. Adv Mater 27:5010–5016

85. Zhang C, An B, Yang L, Wu B, Shi W, Wang YC, Long LS, Wang C, Lin W (2016) Sulfur-doping achieves efficient oxygen reduction in pyrolyzed zeolitic imidazolate frameworks. J Mater Chem A 4:4457–4463

86. Li X, Jiang Q, Dou S, Deng L, Huo J, Wang S (2016) ZIF-67-derived Co-NC@CoP-NC nanopolyhedra as an efficient bifunctional oxygen electrocatalyst. J Mater Chem A 4:15836–15840

87. You S, Gong X, Wang W, Qi D, Wang X, Chen X, Ren N (2016) Enhanced cathodic oxygen reduction and power production of microbial fuel cell based on noble-metal-free electrocatalyst derived from metal-organic frameworks. Adv Energy Mater 6:1501497

88. Li Z, Shao M, Zhou L, Zhang R, Zhang C, Wei M, Evans DG, Duan X (2016) Directed growth of metal-organic frameworks and their derived carbon-based network for efficient electrocatalytic oxygen reduction. Adv Mater 28:2337–2344

89. Meng F, Zhong H, Bao D, Yan J, Zhang X (2016) In situ coupling of strung Co$_4$N and intertwined N–C fibers toward free-standing bifunctional cathode for robust, efficient, and flexible Zn–air batteries. J Am Chem Soc 138:10226–10231

90. Yin P, Yao T, Wu Y, Zheng L, Lin Y, Liu W, Ju H, Zhu J, Hong X, Deng Z, Zhou G, Wei S, Li Y (2016) Single cobalt atoms with precise N-coordination as superior oxygen reduction reaction catalysts. Angew Chem Int Ed 55:10800–10805

91. Aijaz A, Masa J, Rösler C, Xia W, Weide P, Botz AJR, Fischer RA, Schuhmann W, Muhler M (2016) Co@Co$_3$O$_4$ encapsulated in carbon nanotube-grafted nitrogen-doped carbon polyhedra as an advanced bifunctional oxygen electrode. Angew Chem Int Ed 55:4087–4091

92. Ni B, Ouyang C, Xu X, Zhuang J, Wang X (2017) Modifying commercial carbon with trace amounts of ZIF to prepare derivatives with superior ORR activities. Adv Mater 29:1701354

93. Hou YN, Zhao Z, Yu Z, Tang Y, Wang X, Qiu J (2017) Two-dimensional graphene-like N, Co-codoped carbon nanosheets derived from ZIF-67 polyhedrons for efficient oxygen reduction reactions. Chem Commun 53:7840–7843

94. Wei J, Hu Y, Liang Y, Kong B, Zheng Z, Zhang J, Jiang SP, Zhao Y, Wang H (2017) Graphene oxide/core–shell structured metal–organic framework nano-sandwiches and their derived cobalt/N-doped carbon nanosheets for oxygen reduction reactions. J Mater Chem A 5:10182–10189

95. Yang W, Liu X, Chen L, Liang L, Jia J (2017) A metal–organic framework devised Co–N doped carbon microsphere/nanofiber hybrid as a free-standing 3D oxygen catalyst. Chem Commun 53:4034–4037

96. Meng J, Niu C, Xu L, Li J, Liu X, Wang X, Wu Y, Xu X, Chen W, Li Q, Zhu Z, Zhao D, Mai L (2017) General oriented formation of carbon nanotubes from metal–organic frameworks. J Am Chem Soc 139:8212–8221

97. Hou Y, Huang T, Wen Z, Mao S, Cui S, Chen J (2014) Metal–organic framework-derived nitrogen-doped core-shell-structured porous Fe/Fe$_3$C@C nanoboxes supported on graphene sheets for efficient oxygen reduction reactions. Adv Energy Mater 4:1400337

98. Sanetuntikul J, Shanmugam S (2014) Prussian blue-carbon hybrid as a non-precious electrocatalyst for the oxygen reduction reaction in alkaline medium. Electrochim Acta 119:92–98

99. Zhou R, Qiao SZ (2015) An Fe/N co-doped graphitic carbon bulb for high-performance oxygen reduction reaction. Chem Commun 51:7516–7519

100. Wang X, Zou L, Fu H, Xiong Y, Tao Z, Zheng J, Li X (2016) Noble metal-free oxygen reduction reaction catalysts derived from Prussian blue nanocrystals dispersed in polyaniline. ACS Appl Mater Interfaces 8:8436–8444

101. Yang J, Hu J, Weng M, Tan R, Tian L, Yang J, Amine J, Zheng J, Chen H, Pan F (2017) Fe-cluster pushing electrons to N-doped graphitic layers with Fe$_3$C(Fe) hybrid nanostructure to enhance O$_2$ reduction catalysis Zn-air batteries. ACS Appl Mater Interfaces 9:4587–4596

102. Kong A, Lin Q, Mao C, Bu X, Feng P (2014) Efficient oxygen reduction by nanocomposites of heterometallic carbide and nitrogen-enriched carbon derived from the cobalt-encapsulated indium–MOF. Chem Commun 50:15619–15622

103. Lin Q, Bu X, Kong A, Mao C, Zhao X, Bu F, Feng P (2015) New heterometallic zirconium metalloporphyrin frameworks and their heteroatom-activated high-surface-area carbon derivatives. J Am Chem Soc 137:2235–2238

104. Afsahi F, Kaliaguine S (2014) Non-precious electrocatalysts synthesized from metal–organic frameworks. J Mater Chem A 2:12270–12279

105. Volosskiy B, Fei H, Zhao Z, Lee S, Li M, Lin Z, Papandrea B, Wang C, Huang Y, Duan X (2016) Tuning the catalytic activity of a metal–organic framework derived copper and nitrogen co-doped carbon composite for oxygen reduction reaction. ACS Appl Mater Interfaces 8:26769–26774

106. Yuan S, Shui JL, Grabstanowicz L, Chen C, Commet S, Reprogle B, Xu T, Yu L, Liu DJ (2013) A highly active and support-free oxygen reduction catalyst prepared from ultrahigh-surface-area porous polyporphyrin. Angew Chem Int Ed 52:8349–8353

107. Xiang Z, Xue Y, Cao D, Huang L, Chen JF, Dai L (2014) Highly efficient electrocatalysts for oxygen reduction based on 2D covalent organic polymers complexed with non-precious metals. Angew Chem Int Ed 53:2433–2437

108. Wu ZS, Chen L, Liu J, Parvez K, Liang H, Shu J, Sachdev H, Graf R, Feng X, Müllen K (2014) High-performance electrocatalysts for oxygen reduction derived from cobalt porphyrin-based conjugated mesoporous polymers. Adv Mater 26:1450–1455

109. Lin Q, Bu X, Kong A, Mao C, Bu F, Feng P (2015) Heterometal-embedded organic conjugate frameworks from alternating monomeric iron and cobalt metalloporphyrins and their application in design of porous carbon catalysts. Adv Mater 27:3431–3436

110. Olson TS, Pylypenko S, Fulghum JE, Atanassov P (2010) Bifunctional oxygen reduction reaction mechanism on non-platinum catalysts derived from pyrolyzed porphyrins. J Electrochem Soc 157:B54–B63

111. Serov A, Robson MH, Smolnik M, Atanassov P (2012) Templated bi-metallic non-PGM catalysts for oxygen reduction. Electrochim Acta 80:213–218

112. Serov A, Artyushkova K, Atanassov P (2014) Fe-N-C oxygen reduction fuel cell catalyst derived from carbendazim: synthesis, structure, and reactivity. Adv Energy Mater 4:1301735

113. Santoro C, Serov A, Stariha L, Kodali M, Gordon J, Babanova S, Bretschger O, Artyushkova K, Atanassov P (2016) Iron based catalysts from novel low-cost organic precursors for enhanced oxygen reduction reaction in neutral media microbial fuel cells. Energy Environ Sci 9:2346–2353

114. Zhou M, Yang C, Chan KY (2014) Structuring porous iron-nitrogen-doped carbon in a core/shell geometry for the oxygen reduction reaction. Adv Energy Mater 4:1400840

115. Yu Q, Xu J, Wan C, Wu C, Guan L (2015) Porous cobalt–nitrogen-doped hollow graphene spheres as a superior electrocatalyst for enhanced oxygen reduction in both alkaline and acidic solutions. J Mater Chem A 3:16419–16423

116. Silva R, Voiry D, Chhowalla M, Asefa T (2013) Efficient metal-free electrocatalysts for oxygen reduction reaction: polyaniline-derived N- and O-doped mesoporous carbons. J Am Chem Soc 135:7823–7826

117. Cheon JY, Kim T, Choi YM, Jeong HY, Kim MG, Sa YJ, Kim J, Lee Z, Yang TH, Kwon K, Teraski O, Park GG, Adzic RR, Joo SH (2013) Ordered mesoporous porphyrinic carbons with very high electrocatalytic activity for the oxygen reduction reaction. Sci Rep 3:2715

118. Liang HW, Wei W, Wu ZS, Feng X, Müllen K (2013) Mesoporous metal–nitrogen-doped carbon electrocatalysts for highly efficient oxygen reduction reaction. J Am Chem Soc 135:16002–16005

119. Dombrovkis JK, Jeong HY, Fossum K, Terasaki O, Palmqvist AEC (2013) Transition metal ion-chelating ordered mesoporous carbons as noble metal-free fuel cell catalysts. Chem Mater 25:856–861

120. Kong A, Dong B, Zhu X, Kong Y, Zhang J, Shan Y (2013) Ordered mesoporous Fe-porphyrin-like architectures as excellent cathode materials for the oxygen reduction reaction in both alkaline and acidic media. Chem Eur J 19:16170–16175

121. Kong A, Zhu X, Han Z, Yu Y, Zhang Y, Dong B, Shan Y (2014) Ordered hierarchically micro- and mesoporous Fe-N$_x$-embedded graphitic architectures as efficient electrocatalysts for oxygen reduction reaction. ACS Catal 4:1793–1800

122. Yan XH, Xu BQ (2014) Mesoporous carbon material co-doped with nitrogen and iron (Fe–N–C): high-performance cathode catalyst for oxygen reduction reaction in alkaline electrolyte. J Mater Chem A 2:8617–8622

123. Yang DS, Bhattacharjya D, Song MY, Razmjooei F, Ko J, Yang QH, Yu JS (2015) Nitrogen-doped ordered mesoporous carbon with different morphologies for the oxygen reduction reaction: effect of iron species and synergy of textural properties. ChemCatChem 7:2882–2890

124. Cheon JY, Kim K, Sa YJ, Sahgong SH, Hong Y, Woo J, Yim SD, Jeong HY, Kim Y, Joo SH (2016) Graphitic nanoshell/mesoporous carbon nanohybrids as highly efficient and stable bifunctional oxygen electrocatalysts for rechargeable aqueous Na–air batteries. Adv Energy Mater 6:1501794

125. Woo J, Sa YJ, Kim JH, Lee HW, Pak C, Joo SH (2018) Impact of textural properties of mesoporous porphyrinic carbon electrocatalysts on oxygen reduction reaction activity. ChemElectroChem. https://doi.org/10.1002/celc.201800183

126. Niu W, Li L, Liu X, Wang N, Liu J, Zhou W, Tang Z, Chen S (2015) Mesoporous N-doped carbons prepared with thermally removable nanoparticle templates: an efficient electrocatalyst for oxygen reduction reaction. J Am Chem Soc 137:5555–5562

127. Meng FL, Wang ZL, Zhong HX, Wang J, Yan JM, Zhang XB (2016) Reactive multifunctional template-induced preparation of Fe-N-doped mesoporous carbon microspheres towards highly efficient electrocatalysts for oxygen reduction. Adv Mater 28:7948–7955

128. Li JC, Hou PX, Shi C, Zhao SY, Tang DM, Cheng M, Liu C, Cheng HM (2016) Hierarchically porous Fe-N-doped carbon nanotubes as efficient electrocatalyst for oxygen reduction. Carbon 109:632–639

129. Sun T, Wu Q, Zhuo O, Jiang Y, Bu Y, Yang L, Wang X, Hu Z (2016) Manganese oxide-induced strategy to high-performance iron/nitrogen/carbon electrocatalysts with highly exposed active sites. Nanoscale 8:8480–8485

130. Wang B, Wang X, Zou J, Yan Y, Xie S, Hu G, Li Y, Dong A (2017) Simple-cubic carbon frameworks with atomically dispersed iron dopants toward high-efficiency oxygen reduction. Nano Lett 17:2003–2009

131. Song LT, Wu ZY, Zhou F, Liang HW, Yu ZY, Yu SH (2016) Sustainable hydrothermal carbonization synthesis of iron/nitrogen-doped carbon nanofiber aerogels as electrocatalysts for oxygen reduction. Small 12:6398–6406

132. Zhu C, Fu S, Song J, Shi Q, Su D, Engelhard MH, Li X, Xiao D, Li D, Estevez L, Du D, Lin Y (2017) Self-assembled Fe–N-doped carbon nanotube aerogels with single-atom catalyst feature as high-efficiency oxygen reduction electrocatalysts. Small 13:1603407

133. Lu B, Smart TJ, Qin D, Lu JE, Wang N, Chen L, Peng Y, Ping Y, Chen S (2017) Nitrogen and iron-codoped carbon hollow nanotubules as high-performance catalysts toward oxygen reduction reaction: a combined experimental and theoretical study. Chem Mater 29:5617–5628

134. Ahn SH, Klein MJ, Manthiram A (2017) 1D Co- and N-doped hierarchically porous carbon nanotubes derived from bimetallic metal organic framework for efficient oxygen and tri-iodide reduction reactions. Adv Energy Mater 7:1601979

135. Ahn SH, Yu X, Manthiram A (2017) "Wiring" Fe-N$_x$-embedded porous carbon framework onto 1D nanotubes for efficient oxygen reduction reaction in alkaline and acidic media. Adv Mater 29:1606534

136. Ding W, Li L, Xiong K, Wang Y, Li W, Nie Y, Chen S, Qi X, Wei Z (2015) Shape fixing via salt recrystallization: a morphology-controlled approach to convert nanostructured polymer to carbon nanomaterial as a highly active catalyst for oxygen reduction reaction. J Am Chem Soc 137:5414–5420

137. Niu W, Li L, Wang N, Zeng S, Liu J, Zhao D, Chen S (2016) Volatilizable template-assisted scalable preparation of honeycomb-like porous carbons for efficient oxygen electroreduction. J Mater Chem A 4:10820–10827

138. Zhang Y, Huang LB, Jiang WJ, Zhang X, Chen YY, Wei Z, Wan LJ, Hu JS (2016) Sodium chloride-assisted green synthesis of a 3D Fe–N–C hybrid as highly active electrocatalyst for the oxygen reduction reaction. J Mater Chem A 4:7781–7787

139. Chung DY, Kim MJ, Kang N, Yoo JM, Shin H, Kim OH, Sung YE (2017) Low-temperature and gram-scale synthesis of two-dimensional Fe–N–C carbon sheets for robust electrochemical oxygen reduction reaction. Chem Mater 29:2890–2898

140. Xu J, Xin S, Liu JW, Wang JL, Lei Y, Yu SH (2016) Elastic carbon nanotube aerogel meets tellurium nanowires: a binder- and collector-free electrode for Li-Te batteries. Adv Funct Mater 26:3580–3588

141. Brüller S, Liang HW, Kramm UI, Krumpfer JW, Feng X, Müllen K (2015) Bimetallic porous porphyrin polymer-derived non-precious metal electrocatalysts for oxygen reduction reactions. J Mater Chem A 3:23799–23808

142. Zhang R, He S, Lu Y, Chen W (2015) Fe, Co, N-functionalized carbon nanotubes in situ grown on 3D porous N-doped carbon foams as a noble metal-free catalyst for oxygen reduction. J Mater Chem A 3:3559–3567

143. Sahraie NR, Kramm UI, Steinberg J, Zhang Y, Thomas A, Reier T, Paraknowitsch JP, Strasser P (2015) Quantifying the density and utilization of active sites in non-precious metal oxygen electroreduction catalysts. Nat Commun 6:8618

144. Lin L, Yang ZK, Jiang YF, Xu AW (2016) Nonprecious bimetallic (Fe, Mo)–N/C catalyst for efficient oxygen reduction reaction. ACS Catal 6:4449–4454

145. Su CY, Cheng H, Li W, Liu ZQ, Li N, Hou Z, Bai FQ, Zhang HX, Ma TY (2017) Atomic modulation of FeCo–nitrogen–carbon

bifunctional oxygen electrodes for rechargeable and flexible all-solid-state zinc–air battery. Adv Energy Mater 7:1602420

146. Herrmann I, Kramm UI, Radnik J, Fiechter S, Bogdanoff P (2009) Influence of sulfur on the pyrolysis of CoTMPP as electrocatalyst for the oxygen reduction reaction. J Electrochem Soc 156:B1283–B1292

147. Kramm UI, Herrmann I, Fiechter S, Zehl G, Zizak I, Abs-Wurmbach I, Radnik J, Dorbandt I, Bogdanoff P (2009) On the influence of sulphur on the pyrolysis process of FeTMPP-Cl-based electro-catalysts with respect to oxygen reduction reaction (ORR) in acidic media. ECS Trans 25:659–670

148. Kramm UI, Herrmann-Geppert I, Fiechter S, Zehl G, Zizak I, Dorbandt I, Schmeißer D, Bogdanoff P (2014) Effect of iron-carbide formation on the number of active sites in Fe–N–C catalysts for the oxygen reduction reaction in acidic media. J Mater Chem A 2:2663–2670

149. Ferrandon M, Kropf AJ, Myers DJ, Artyushkova K, Kramm U, Bogdanoff P, Wu G, Johnston CM, Zelenay P (2012) Multi-technique characterization of a polyaniline–iron–carbon oxygen reduction catalyst. J Phys Chem C 116:16001–16013

150. Chang Y, Hong F, He C, Zhang Q, Liu J (2013) Nitrogen and sulfur dual-doped non-noble catalyst using fluidic acrylonitrile telomer as precursor for efficient oxygen reduction. Adv Mater 25:4794–4799

151. Sahraie NR, Paraknowitsch JP, Göbel C, Thomas A, Strasser P (2014) Noble-metal-free electrocatalysts with enhanced ORR performance by task-specific functionalization of carbon using ionic liquid precursor systems. J Am Chem Soc 136:14486–14497

152. Wang YC, Lai YJ, Song L, Zhou ZY, Liu JG, Wang Q, Yang XD, Chen C, Shi W, Zheng YP, Rauf M, Sun SG (2015) S-doping of an Fe/N/C ORR catalyst for polymer electrolyte membrane fuel cells with high power density. Angew Chem Int Ed 54:9907–9910

153. Chen C, Yang XD, Zhou ZY, Lai YJ, Rauf M, Wang Y, Pan J, Zhuang L, Wang Q, Wang YC, Tian N, Zhang XS, Sun SG (2015) Aminothiazole-derived N,S,Fe-doped graphene nanosheets as high performance electrocatalysts for oxygen reduction. Chem Commun 51:17092–17095

154. Hu K, Tao L, Liu D, Huo J, Wang S (2016) Sulfur-doped Fe/N/C nanosheets as highly efficient electrocatalysts for oxygen reduction reaction. ACS Appl Mater Interfaces 8:19379–19385

155. Oh S, Kim JH, Kim MJ, Nam DH, Park JY, Cho EA, Kwon HS (2016) Synergetic effects of edge formation and sulfur doping on the catalytic activity of a graphene-based catalyst for the oxygen reduction reaction. J Mater Chem A 4:14400–14407

156. Elumeeva K, Ren J, Antonietti M, Fellinger TP (2015) High surface iron/cobalt-containing nitrogen-doped carbon aerogels as non-precious advanced electrocatalysts for oxygen reduction. ChemElectroChem 2:584–591

157. Cheon JY, Kim JH, Kim JH, Goddeti KC, Park JY, Joo SH (2014) Intrinsic relationship between enhanced oxygen reduction reaction activity and nanoscale work function of doped carbons. J Am Chem Soc 136:8875–8878

158. Kramm UI, Herrmann-Geppert I, Behrends J, Lips K, Fiechter S, Bogdanoff P (2016) On an easy way to prepare metal–nitrogen doped carbon with exclusive presence of MeN$_4$-type sites active for the ORR. J Am Chem Soc 138:635–640

159. Sa YJ, Seo DJ, Woo J, Lim JT, Cheon JY, Yang SY, Lee JM, Kang D, Shin TJ, Shin HS, Jeong HY, Kim CS, Kim MG, Kim TY, Joo SH (2016) A general approach to preferential formation of active Fe–N$_x$ sites in Fe–N/C electrocatalysts for efficient oxygen reduction reaction. J Am Chem Soc 138:15046–15056

160. Shang L, Yu H, Huang X, Bian T, Shi R, Zhao Y, Waterhouse GIN, Wu LZ, Tung CH, Zhang T (2016) Well-dispersed ZIF-derived Co,N-co-doped carbon nanoframes through

161. Collman JP, Devaraj NK, Decréau RA, Yang Y, Yan YL, Ebina W, Eberspacher TA, Chidsey CED (2007) A cytochrome c oxidase model catalyzes oxygen to water reduction under rate-limiting electron flux. Science 315:1565–1568

162. Bouwkamp-Wijnoltz AL, Visscher W, van Veen JAR, Boellaard E, van der Kraan AM, Tang SC (2002) On active-site heterogeneity in pyrolyzed carbon-supported iron porphyrin catalysts for the electrochemical reduction of oxygen: an in situ Mössbauer study. J Phys Chem B 106:12993–13001

163. Kramm UI, Abs-Wurmbach I, Herrmann-Geppert I, Radnik J, Fiechter S, Bogdanoff P (2011) Influence of the electron density of FeN$_4$-centers towards the catalytic activity of pyrolyzed FeTMPPCl-based ORR-electrocatalysts. J Electrochem Soc 158:B69–B78

164. Jia Q, Ramaswamy N, Hafiz H, Tylus U, Strickland K, Wu G, Barbiellini B, Bansil A, Holby EF, Zelenay P, Mukerjee S (2015) Experimental observation of redox-induced Fe–N switching behavior as a determinant role for oxygen reduction activity. ACS Nano 9:12496–12505

165. Jiang Y, Lu Y, Lv X, Han D, Zhang Q, Niu L, Chen W (2013) Enhanced catalytic performance of Pt-free iron phthalocyanine by graphene support for efficient oxygen reduction reaction. ACS Catal 3:1263–1271

166. Lv G, Cui L, Wu Y, Liu Y, Pu T, He X (2013) A novel cobalt tetranitrophthalocyanine/graphene composite assembled by an in situ solvothermal synthesis method as a highly efficient electrocatalyst for the oxygen reduction reaction in alkaline medium. Phys Chem Chem Phys 15:13093–13100

167. Levy N, Mahammed A, Kosa M, Major DT, Gross Z, Elbaz L (2015) Metallocorroles as nonprecious-metal catalysts for oxygen reduction. Angew Chem Int Ed 54:14080–14084

168. Tang H, Yin H, Wang J, Yang N, Wang D, Tang Z (2013) Molecular architecture of cobalt porphyrin multilayers on reduced graphene oxide sheets for high-performance oxygen reduction reaction. Angew Chem Int Ed 52:5585–5589

169. Hijazi I, Bourgeteau T, Cornut R, Morozan A, Filoramo A, Leroy J, Derycke V, Jousselme B, Campidelli S (2014) Carbon nanotube-templated synthesis of covalent porphyrin network for oxygen reduction reaction. J Am Chem Soc 136:6348–6354

170. Xi Y, Wei PJ, Wang RC, Liu JG (2015) Bio-inspired multinuclear copper complexes covalently immobilized on reduced graphene oxide as efficient electrocatalysts for the oxygen reduction reaction. Chem Commun 51:7455–7458

171. Collman JP, Denisevich P, Konai Y, Marrocco M, Koval C, Anson FC (1980) Electrode catalysis of the four-electron reduction of oxygen to water by dicobalt face-to-face porphyrins. J Am Chem Soc 102:6027–6036

172. Cao R, Thapa R, Kim H, Xu X, Kim MG, Li Q, Park N, Liu M, Cho J (2013) Promotion of oxygen reduction by a bio-inspired tethered iron phthalocyanine carbon nanotube-based catalyst. Nat Commun 4:2076

173. Wei PJ, Yu GQ, Naruta Y, Liu JG (2014) Covalent grafting of carbon nanotubes with a biomimetic heme model compound to enhance oxygen reduction reactions. Angew Chem Int Ed 53:6659–6663

174. Liu JG, Shimizu Y, Ohta T, Naruta Y (2010) Formation of an end-on ferric peroxo intermediate upon one-electron reduction of a ferric superoxo heme. J Am Chem Soc 132:3672–3673

175. Chlistunoff J, Sansiñena JM (2014) Effects of axial coordination of the metal center on the activity of iron tetraphenylporphyrin as a nonprecious catalyst for oxygen reduction. J Phys Chem C 118:19139–19149

176. Han J, Sa YJ, Shim Y, Choi M, Park N, Joo SH, Park S (2015) Coordination chemistry of [Co(acac)$_2$] with N-doped graphene:

implications for oxygen reduction reaction reactivity of organo-metallic Co-O$_4$-N species. Angew Chem Int Ed 54:12622–12626

177. Chung HT, Won JH, Zelenay P (2013) Active and stable carbon nanotube/nanoparticle composite electrocatalyst for oxygen reduction. Nat Commun 4:1922

178. Zhong X, Liu L, Wang X, Yu H, Zhuang G, Mei D, Li X, Wang J (2014) A radar-like iron based nanohybrid as an efficient and stable electrocatalyst for oxygen reduction. J Mater Chem A 2:6703–6707

179. Lin L, Zhu Q, Xu AW (2014) Noble-metal-free Fe–N/C catalyst for highly efficient oxygen reduction reaction under both alkaline and acidic conditions. J Am Chem Soc 136:11027–11033

180. Zhu Y, Zhang B, Liu X, Wang DW, Su DS (2014) Unraveling the structure of electrocatalytically active Fe–N complexes in carbon for the oxygen reduction reaction. Angew Chem Int Ed 53:10673–10677

181. Xiao M, Zhu J, Feng L, Liu C, Xing W (2015) Meso/microporous nitrogen-doped carbon architectures with iron carbide encapsulated in graphitic layers as an efficient and robust catalyst for the oxygen reduction reaction in both acidic and alkaline solutions. Adv Mater 27:2521–2527

182. Wu H, Li H, Zhao X, Liu Q, Wang J, Xiao J, Xie S, Si R, Yang F, Miao S, Guo X, Wang G, Bao X (2016) Highly doped and exposed Cu(I)–N active sites within graphene towards efficient oxygen reduction for zinc–air batteries. Energy Enrivon Sci 9:3736–3745

183. Jiang WJ, Gu L, Li L, Zhang Y, Zhang X, Zhang LJ, Wang JQ, Hu JS, Wei Z, Wan LJ (2016) Understanding the high activity of Fe–N–C electrocatalysts in oxygen reduction: Fe/Fe$_3$C

184. Guan BY, Yu L, Lou XW (2016) A dual-metal–organic-framework derived electrocatalyst for oxygen reduction. Energy Environ Sci 9:3092–3096

185. Gupta S, Zhao S, Ogoke O, Lin Y, Xu H, Wu G (2017) Engineering favorable morphology and structure of Fe-N-C oxygen-reduction catalysts through tuning of nitrogen/carbon precursors. ChemSusChem 10:774–785

186. Fu X, Zamani P, Choi JY, Hassan FM, Jiang G, Higgins DC, Zhang Y, Hoque MA, Chen Z (2017) In situ polymer graphenization ingrained with nanoporosity in a nitrogenous electrocatalyst boosting the performance of polymer-electrolyte-membrane fuel cells. Adv Mater 29:1604456

187. Rauf M, Zhao YD, Wang YC, Zheng YP, Chen C, Yang XD, Zhou ZY, Sun SG (2016) Insight into the different ORR catalytic activity of Fe/N/C between acidic and alkaline media: protonation of pyridinic nitrogen. Electrochem Commun 73:71–74

188. Dong G, Fang M, Wang H, Yip S, Cheung HY, Wang F, Wong CY, Chu ST, Ho JC (2015) Insight into the electrochemical activation of carbon-based cathodes for hydrogen evolution reaction. J Mater Chem A 3:13080–13086

189. Chen R, Yang C, Cai W, Wang HY, Miao J, Zhang L, Chen S, Liu B (2017) Use of platinum as the counter electrode to study the activity of nonprecious metal catalysts for the hydrogen evolution reaction. ACS Energy Lett 2:1070–1075

190. Zhou R, Zheng Y, Jaroniec M, Qiao SZ (2016) Determination of the electron transfer number for the oxygen reduction reaction: from theory to experiment. ACS Catal 6:4720–4728